J. Fluid Mech. (1994), *vol.* 262, *pp.* 171–204

A new computational method for the solution of flow problems of microstructured fluids. Part 2. Inhomogeneous shear flow of a suspension

By ANDREW J. SZERI[1] AND L. GARY LEAL[2]

[1] Department of Mechanical and Aerospace Engineering, University of California, Irvine, CA 92717-3975, USA

[2] Department of Chemical and Nuclear Engineering, University of California, Santa Barbara, CA 93106, USA

(Received 26 June 1992 and in revised form 27 August 1993)

A numerical investigation is conducted into the flow of a dilute suspension of rigid rod-like particles between parallel flat plates, driven by a uniform pressure gradient. The particles are assumed to be small relative to lengthscales of the flow with the effect that particle orientations evolve according to the local velocity gradient; the particles are also assumed to be small in an absolute sense, with the consequence that Brownian motions are of consequence. The calculations are performed using a novel approach, with a theoretical basis that has been developed previously in a companion paper (Szeri & Leal 1992). The new approach permits one to solve flow problems of microstructured fluids (such as suspensions, liquid crystals, polymer solutions and melts) without 'pre-averaging' or closure approximations. In the present work, the new approach is used to expose previously unknown pathological, *non-physical* predictions in various constitutive models derived using closure approximations. This appears to have passed unnoticed in prior work. In addition, the new approach is shown to possess several computational advantages. The determination of the orientation distribution of particles is self-adaptive; this leads, in effect, to a very efficient solution of the associated Smoluchowski (or Fokker–Planck) equation. Moreover, the new approach is highly suited to parallel (and vector) implementation on modern computers. These issues are explored in detail in the context of the example flow.

1. Introduction

In this paper, we investigate a specific flow of a dilute suspension of rigid, rod-like particles which has a spatially inhomogeneous velocity field, is time-dependent and involves Brownian motions of the particles. The suspension is only one example of the general class of microstructured fluids that includes polymer solutions and melts, liquid crystals, colloidal dispersions, etc. The primary goal of the present work is to implement a new technique for the solution of flow problems of these materials, which has a theoretical basis that was carefully developed in a companion paper, Szeri & Leal (1992, hereinafter referred to as I). As our technique does not require 'pre-averaging' or closure approximations, we have an opportunity to test some commonly made closure approximations used to develop constitutive models for this type of material. Our technique exposes previously unknown *non-physical* behaviour in these models.

A secondary goal of the present work is to evaluate this first numerical implementation of our technique. The two principal features on which we focus are (i)

the self-adaptive nature of the discretization in which the evolving microstructure is followed, and (ii) the extent to which our reformulation of the governing equations allows us to take advantage of parallel (and vector) computation. In the evaluation of the algorithm, we observe that our implementation of the new technique requires 1–2 orders of magnitude fewer unknowns than a recent comparable calculation by Kamal & Mutel (1989), which uses a standard non-self-adaptive technique to track the evolving microstructure. In addition, our implementation of the new technique has a parallel efficiency (speed-up/number of processors) of nearly 70%, as a consequence of the fact that the microstructure at each material point of interest can be updated simultaneously and independently by a dedicated processor (each operating in vector mode).

We focus on dilute suspensions of rigid rod-like particles. The particles are assumed to be small relative to lengthscales of the flow; in addition, we assume that the particles follow the same paths through the flow as fluid particles. Hence, the influence of the flow on the orientation of a particle is felt through the local velocity gradient tensor of the flow. As well as the influence of the flow on the particles, we assume that rotational Brownian motions of the particles are important. Mathematically, these phenomena are described by the evolution equations for the local orientation distribution function of a dilute suspension of rigid, rod-like (axisymmetric) particles:

$$\frac{\mathrm{d}}{\mathrm{d}t}\boldsymbol{R} = \boldsymbol{\Omega}\cdot\boldsymbol{R} + G[\boldsymbol{E}\cdot\boldsymbol{R} - \boldsymbol{E}:\boldsymbol{RRR}] - D_R\nabla(\log f), \tag{1.1a}$$

$$\frac{\partial f}{\partial t} + \nabla\cdot(f\dot{\boldsymbol{R}}) = 0. \tag{1.1b}$$

For background on (1.1), the interested reader may consult Larson (1988) or Bird *et al.* (1987), among other works. In (1.1*a*), the orientation of a particle, specified by a vector $\boldsymbol{R}$ parallel to the axis of symmetry, evolves according to the local vorticity tensor $\boldsymbol{\Omega}$ and rate-of-strain tensor $\boldsymbol{E}$. The shape factor G accounts for the inefficiency of rotation of particles of finite aspect ratio in straining flows; G lies normally between the extremes 0 (spherical particle) and 1 (infinite-aspect-ratio fibre). The Brownian motion of the particle is modelled as a diffusive process by the last term in (1.1*a*), that involves the Brownian diffusivity D_R and the orientation distribution function f. The gradient in this term is an operator in orientation space. The orientation distribution function f evolves according to the Fokker–Planck equation (1.1*b*), which describes the conservation of probability in orientation space.

In a realistic flow problem in which the velocity gradient tensor is time-dependent and spatially inhomogeneous, the local orientation distribution function must be found from (1.1) throughout the flow field. In addition, the state of stress throughout the suspension depends on the local orientation distribution of particles through the second and fourth moments of the distribution function, i.e.

$$\langle\boldsymbol{RR}\rangle(t) \equiv \int (\boldsymbol{R}\otimes\boldsymbol{R}) f(\boldsymbol{R}, t)\,\mathrm{d}^2\boldsymbol{R},$$

$$\langle\boldsymbol{RRRR}\rangle(t) \equiv \int (\boldsymbol{R}\otimes\boldsymbol{R}\otimes\boldsymbol{R}\otimes\boldsymbol{R}) f(\boldsymbol{R}, t)\,\mathrm{d}^2\boldsymbol{R}.$$

It is worth emphasizing that one requires only the relevant moments of the local orientation distribution function rather than the local orientation distribution function itself when computing a flow. This practical realization has led to a number of attempts

to compute moments of distribution functions directly. However, in suspensions of rigid rod-like particles, and in most other types of microstructured fluids, one must make strong approximations in order to obtain a closed set of evolution equations for the moment of interest. The development of direct moment evolution equations, closure approximations, and the shortcomings of this approach are discussed at length in I.

The major shortcomings of the standard approach to solving flow problems of microstructured fluids led us to consider a new approach with a basis more closely related to the physics of the problem than the approach of making a closure approximation. The details of the theoretical development are given in I. The basic idea is to reformulate the equations for the orientation distribution function of a material point in a way that is Lagrangian in *orientation space* (in the case of rigid orientable particles). Mathematically, the Lagrangian and Eulerian forms of the distribution function for a material point of fixed identity are related by the definition

$$f^*(t; \boldsymbol{R}_0) \equiv f(t, \boldsymbol{R})|_{\boldsymbol{R}=\hat{\boldsymbol{R}}(t;\boldsymbol{R}_0)}.$$

Here, $\hat{\boldsymbol{R}}(t; \boldsymbol{R}_0)$ is the solution of the associated microdynamical equation (1.1*a*) with initial condition $\boldsymbol{R}_0$. Hence, the Lagrangian form of the distribution function tracks the evolving orientation distribution associated with a given particle and not with a given orientation.

From the conservation statement for the conventional Eulerian form of the distribution function (1.1*b*), we derived in I the conservation statement for the new, Lagrangian form. This equation is

$$\frac{f^*(t; \boldsymbol{R})}{f^*(0; \boldsymbol{R}_0)} = \frac{1}{\det(\nabla_0 \hat{\boldsymbol{R}}(t; \boldsymbol{R}_0))}. \tag{1.2}$$

Moments may be recast in the reference configuration, by taking the point of view that (1.2) is really an expression of a coordinate transformation for each material point; hence for an initially isotropic orientation distribution ($f(\boldsymbol{R}, 0) = 1/4\pi$), we have

$$\langle \boldsymbol{RR} \rangle(t) = \int f^*(t; \boldsymbol{R}_0)\, \boldsymbol{R} \otimes \boldsymbol{R}\, \mathrm{d}^2\boldsymbol{R}$$

$$= \frac{1}{4\pi} \int \hat{\boldsymbol{R}}(t; \boldsymbol{R}_0) \otimes \hat{\boldsymbol{R}}(t; \boldsymbol{R}_0)\, \mathrm{d}^2\boldsymbol{R}_0.$$

This same technique was used by Kuzuu & Doi (1980) and earlier by Okagawa, Cox & Mason (1973) in studies of suspension mechanics without Brownian motions. The same idea works well when Brownian motions are included, as in the present work. This equation, and the similar expression for the fourth moment, turn out to be extremely efficient expressions for the computation of the moments we require. In addition, discretization of the reference configuration (which is known) determines the order of accuracy of approximation of the integral. The second use of (1.2) is in the computation of the Brownian term of (1.1*a*). In I, we show that (1.2) may be used to rewrite (1.1*a*) as a single partial differential equation for the map between reference (the expression for the diffusive term of which applies when the initial orientation distribution is isotropic) and deformed configurations $\hat{\boldsymbol{R}}(t; \boldsymbol{R}_0)$:

$$\frac{\partial}{\partial t}\hat{\boldsymbol{R}} = \boldsymbol{\Omega} \cdot \hat{\boldsymbol{R}} + G[\boldsymbol{E} \cdot \hat{\boldsymbol{R}} - \boldsymbol{E} : \hat{\boldsymbol{R}}\hat{\boldsymbol{R}}\hat{\boldsymbol{R}}] - D_R \det(\nabla_0 \hat{\boldsymbol{R}})\, \nabla \left[\frac{1}{\det(\nabla_0 \hat{\boldsymbol{R}})}\right]. \tag{1.3}$$

In a numerical implementation of this technique, we solve for a discretized form of the coordinate map $\hat{\boldsymbol{R}}(t; \boldsymbol{R}_0)$. This is mathematically equivalent to integration of the Fokker–Planck equation. However, numerically, the technique we have described has important advantages.

Our reformulation of the governing equations allows for the determination of the discretized form of the coordinate map in a *self-adaptive* way. We simply release a set of particles with the initial distribution of orientations (which must be known), and let their orientations evolve in the flow in a natural way, according to (1.3). For this reason, we shall only require a relatively coarse resolution in the discretized form of the coordinate map using our technique, compared to the fine resolution required for a Fokker–Planck solver in order to obtain the same accuracy in computation of moments and stresses in the flow.

Relative to direct integration of moment evolution equations, however, the advantage of our technique is not speed of solution, but rather faithful solution of the governing equations. We require no approximation to close the governing equations. Therefore, the technique we propose will be useful in situations where closure approximations are known to be problematic, or in situations where reasonable closure approximations have not been developed.

The flow we have chosen to analyse is pressure-driven flow between parallel flat plates. This flow is attractive for many reasons: the start-up problem is time-dependent; both the unsteady and steady problems have spatially inhomogeneous velocity gradients; the solution for a pure Newtonian fluid is well known; and finally experiments can easily be undertaken in order to compare physical data to the predictions of the calculations. There is, however, one aspect of our technique that is not tested by the example flow we consider here. In the solution of a general flow problem by the double-Lagrangian technique, the particle contribution to the stress would be computed at a large number of material points in the flow. In other words, we would calculate the particle contribution to the stress in a way that is Lagrangian in physical space. This information would then have to be transferred to the macroscopic flow equations, which would presumably be solved using a standard, Eulerian technique. For this step, it would be necessary to develop efficient and accurate approximations for the divergence of the stress, given stress values at a number of non-uniformly spaced material points. In contrast, for the example flow of the present work, particle paths are unimportant owing to translation invariance in the flow direction. Future work will focus on examples in which the Lagrangian aspect of the particle paths must be considered.

The plan of the remainder of the paper is as follows. In §2 we give the macroscopic equations for the flowing suspension, specialized for our example flow. The particle contribution to the stress is left as a body force, to be computed by our new technique. In §3, we then outline our numerical solution procedures. The results of example calculations for various values of the dimensionless parameters are given in §4. These results are then compared in §5 with corresponding predictions obtained using some popular closure approximations to derive moment equations. We find that the moment evolution equations predict non-physical behaviour in some instances. Finally, in §6, we summarize our conclusions. In two Appendices, we consider (A) an alternative discretization of (1.3) which fails, and (B) tests of the numerical technique.

2. Formulation of the flow problem

In this section, we outline the numerical problem and our implementation of the double-Lagrangian technique.

2.1. *Macroscopic equations*

We are interested in the case of parallel unidirectional flow of the suspension between flat plates. To be specific, let the plates lie at $y = h$, and $y = -h$, with the flow occurring in the x-direction. We assume that the suspension is initially quiescent, with the microstructure characterized by an isotropic distribution of orientations. The isotropic initial distribution of orientations would arise, for example, owing to the action of Brownian motion over $-\infty < t < 0$. At time $t = 0$, a spatially uniform pressure gradient $\partial p/\partial x(t)$ is applied.

The suspension must satisfy the macroscopic balance of linear momentum and of continuity. These equations are

$$\frac{\partial \boldsymbol{u}}{\partial t} + \boldsymbol{u}\cdot\boldsymbol{\nabla}\boldsymbol{u} = -\frac{1}{\rho}\boldsymbol{\nabla} p_s + \frac{\eta_s}{\rho}\nabla^2\boldsymbol{u} + \frac{1}{\rho}\boldsymbol{\nabla}\cdot\boldsymbol{\tau}^p, \tag{2.1}$$

$$\boldsymbol{\nabla}\cdot\boldsymbol{u} = 0, \tag{2.2}$$

where $\boldsymbol{u}$ is the velocity, ρ is the density of the solvent, p_s is the pressure due to the incompressibility of the solvent, and η_s is the solvent viscosity. One may regard the macroscopic variables that appear in (2.1) as spatial averages of the local microscopic variables. In (2.1), we have partitioned the stress into solvent and particle contributions:

$$\boldsymbol{\tau} = \boldsymbol{\tau}^s + \boldsymbol{\tau}^p,$$

where the solvent (Newtonian) contribution is

$$\boldsymbol{\tau}^s = -p_s\boldsymbol{I} + 2\eta_s\boldsymbol{E}.$$

The boundary conditions on the velocity field are: $v = 0$ and $u = 0$ on $y = \pm h$.

There are a number of simplifications that result from the symmetry of the problem. Because the equations, the domain and the boundary conditions are invariant in the x- and z-directions, we expect that the solutions will be independent of x and z; thus we take $\partial/\partial x = 0$ and $\partial/\partial z = 0$. The exception is that we allow a uniform pressure gradient to exist in the x-direction. Under these assumptions, the continuity equation (2.2) simplifies to $\partial v/\partial y = 0$. The no-slip boundary conditions on velocity require $v(y = \pm h) = 0$; hence $v = 0$ everywhere.

The symmetries $\partial/\partial x = 0$ and $\partial/\partial z = 0$ may be used to simplify the balance of linear momentum also. The y-component of the balance of linear momentum (2.1) simplifies to

$$\frac{\partial p_s}{\partial y} = \frac{\partial \tau^p_{yy}}{\partial y}.$$

Thus, the solvent pressure gradient serves to balance the particle contribution to the normal stress in the y-direction. The x-component of the balance of linear momentum (2.1) becomes

$$\frac{\partial u}{\partial t} = -\frac{1}{\rho}\frac{\partial p_s}{\partial x} + \frac{\eta_s}{\rho}\frac{\partial^2 u}{\partial y^2} + \frac{1}{\rho}\frac{\partial}{\partial y}\tau^p_{xy} + \frac{1}{\rho}\frac{\partial}{\partial x}\tau^p_{xx}. \tag{2.3a}$$

It is this equation that must be solved for u.

The boundary conditions for (2.3*a*) are

$$\frac{\partial u}{\partial y}(y=0)=0, \quad u(y=h)=0. \tag{2.3b}$$

Here we have used the spatial symmetry of the problem about the plane $y=0$ to formulate a reduced problem on the half-domain to $0 \leqslant y \leqslant h$.

2.2. *The particle contribution to the stress*

The particle contribution to the stress at a point in the suspension may be written as

$$\boldsymbol{\tau}^p = -\phi P_0 \boldsymbol{I} + 2\mu_0 \phi \boldsymbol{E} + \mu_1 \phi D_R \langle \boldsymbol{RR} \rangle + \mu_2 \phi \boldsymbol{E} : \langle \boldsymbol{RRRR} \rangle + 2\mu_3 \phi [\boldsymbol{E} \cdot \langle \boldsymbol{RR} \rangle + \langle \boldsymbol{RR} \rangle \cdot \boldsymbol{E}], \tag{2.4}$$

where ϕ is the volume fraction of particles, the constants $\mu_i (i = 0, 3)$ are given in terms of the aspect ratio of the particles and the solvent viscosity, and P_0 is a pressure field due to the presence of the particles. In the expression for the particle contribution to the stress, the constants $\mu_i (i = 0, 3)$ are given by Giesekus (1962) when the particles are ellipsoids of revolution; see also Hinch & Leal (1976), and Lipscomb *et al.* (1988). These constants are uniquely determined by the aspect ratio of the particles when the particles are spheroids.

Owing to the translational invariance in the x-direction, we have

$$\frac{1}{\rho}\frac{\partial}{\partial x}\tau^p_{xx} = -\frac{1}{\rho}\frac{\partial(\phi P_0)}{\partial x}.$$

Hereafter, we combine the solvent and particle pressures as $p = p_s + \phi P_0$. Hence, the balance of linear momentum (2.3*a*) simplifies to the form

$$\frac{\partial u}{\partial t} = -\frac{1}{\rho}\frac{\partial p}{\partial x} + \frac{\eta_s}{\rho}\frac{\partial^2 u}{\partial y^2} + \frac{1}{\rho}\frac{\partial}{\partial y}\tau^p_{xy}, \tag{2.5}$$

and we require only the x, y component of the particle contribution to the stress.

2.3. *Non-dimensionalization*

The problem finally reduces, then, to solving (2.5) with the shear-stress component of the particle stress calculated from (2.4), and the moments of the distribution function obtained by solving (1.1 *a*, *b*) for the distribution function. In the next section, we shall discuss some details of the solution procedure. First, however, it is useful to obtain the governing equations in dimensionless form. This forces us to think carefully about the important physical phenomena, and the characteristic scales that specify them.

We begin by simply adopting the scales that would be relevant for start-up flow of a Newtonian fluid. In particular, as a lengthscale for the macroscopic variables, we use the half-width of the channel, h, and as a timescale we use the viscous diffusion timescale, $t_{Diff} = h^2/\nu_s$. The velocity scale u_{cl} is the (fully developed) centreline velocity of a pure Newtonian fluid flowing under the same conditions. These scales serve to define non-dimensional variables t^*, u^*, and x^*. In addition, we suppose that the pressure and stress components are all characterized by the viscous stress scaling, $\eta_s u_{cl}/h$. With these choices, the momentum equation (2.5) becomes

$$\frac{\partial u^*}{\partial t^*} = -\frac{\partial p^*}{\partial x^*} + \frac{\partial^2 u^*}{\partial y^{*2}} + \frac{\partial \tau^{p*}_{xy}}{\partial y^*}, \tag{2.6}$$

while the particle-stress contribution is

$$\tau_{xy}^{p*} = \frac{\tau_{xy}^{p}}{\eta_s u_{cl}/h} = \phi\frac{\mu_0}{\eta_s}\frac{\partial u^*}{\partial y^*} + \phi\frac{\mu_1}{\eta_s}\frac{1}{Pe}\langle RR\rangle_{xy} + \phi\frac{\mu_2}{\eta_s}\frac{\partial u^*}{\partial y^*}\langle RRRR\rangle_{xxyy} + \phi\frac{\mu_3}{\eta_s}\frac{\partial u^*}{\partial y^*}[\langle RR\rangle_{xx} + \langle RR\rangle_{yy}], \quad (2.7)$$

and the governing equation (1.1) for the distribution function f can be expressed in the form

$$Sc\frac{\partial f}{\partial t^*} + \nabla\cdot[Pe\{\Omega^*\cdot\boldsymbol{R} + G[\boldsymbol{E}^*\cdot\boldsymbol{R} - \boldsymbol{E}^*:\boldsymbol{RRR}]\}f - \nabla f] = 0. \quad (2.8)$$

The dimensionless parameters that appear in these equations are the volume fraction of particles ϕ, the ratios of the material parameters μ_0/η_s, μ_1/η_s, μ_2/η_s and μ_3/η_s which are all $O(1)$, and the two parameters

$$Sc = \nu_s/(h^2 D_R) \quad (2.9)$$

which we denote as the Schmidt number, and

$$Pe = u_{cl}/(hD_R) \quad (2.10)$$

which is the Péclet number for rotational Brownian diffusion.

It can be seen that the Péclet number determines the relative importance of the advection term in (2.8) relative to diffusion. Since it is the flow effect that tends to drive the suspension towards an anisotropic orientation state, while diffusion tends to maintain a state of random (or isotropic) orientation, the magnitude of the Péclet number determines the degree of anisotropy. At steady state, it is the only dimensionless parameter that plays a role in determining the suspension behaviour. In a transient start-up flow, the details of the evolution of the orientation distribution also depend upon the ratio of timescales represented by the Schmidt number. These are the viscous diffusion scale which determines the timescale for start-up of the motion of the suspending fluid, and the rotational diffusion timescale D_R^{-1}.

Although the use of Péclet and Schmidt numbers seems quite natural for the specific problem of start-up flow of a suspension of non-spherical Brownian particles, it is worthwhile to remember that this is but one example of the general class of viscoelastic fluids, and to discuss briefly how the present parameterization is related to that which would normally be used for viscoelastic fluids. In this context, the suspension exhibits a single relaxation timescale, D_R^{-1}, for return from an anisotropic to an isotropic (equilibrium) state. As we have noted earlier, the degree of anisotropy at steady state is determined by the magnitude of the local (or characteristic) velocity gradient relative to D_R, namely Pe. This parameter would also be known as the *Weissenberg number Wi* in a normal viscoelastic flow problem – i.e. the velocity gradient non-dimensionalized with the relaxation time of the fluid. The only other timescale in the problem is that for evolution of the suspending fluid velocity profile, namely h^2/ν_s. Comparison of this timescale with the natural (viscoelastic) relaxation timescale of the fluid, namely D_R^{-1}, determines the relative importance of memory effects in the flow. The ratio of these two timescales, which we denote above as the Schmidt number, would normally be called the *Deborah number* in viscoelastic flows.

The use of Weissenberg and Deborah numbers as described above is consistent with 'normal' rheological understanding of the significance of these parameters. However,

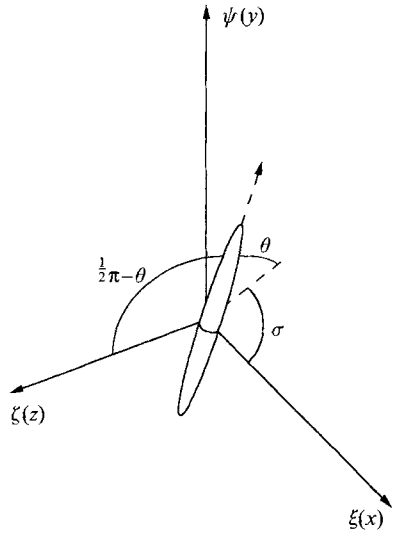

FIGURE 1. Definition sketch for the modified spherical coordinates used to describe the state of a microstructural element. The angle σ is measured in the $\xi-\psi$ $(x-y)$ plane from the ξ-axis; the angle θ is measured from the $\xi-\psi$ plane towards the ζ-axis.

in start-up of a steady flow like that considered here, it is common to ignore the existence of a distinct internal timescale for vorticity diffusion in the solvent (effectively assuming that the solvent responds instantaneously to motion of boundaries, or to onset of a pressure gradient). Then, in a 'steady' problem like start-up of channel flow with a constant pressure gradient after $t = 0$, it has become common practice to use Weissenberg and Deborah numbers interchangeably, both based on the relaxation timescale of the fluid, and the characteristic steady shear rate, $\dot{\gamma}$, and to assume that it is only a problem like an oscillating shear flow with an imposed timescale that one needs to distinguish *De* and *Wi*. For example, if $u = \dot{\gamma}(t)\, y$ and $\dot{\gamma}(t) = \dot{\gamma}_0 \sin \omega t$, then $Wi = \dot{\gamma}_0 \lambda$ whereas $De = \omega\lambda$, with λ being the longest ('principle') relaxation timescale for the fluid. In this case, it is clear that *Wi* provides a measure of the expected degree of anisotropy, and *De* provides a measure of the importance of memory effects. Our formulation of the present problem only differs from the usual formulation in that we assume that the timescale h^2/ν_s is not zero relative to the relaxation time λ (i.e. to D_R^{-1}), and thus our Deborah (or Schmidt) number involves h^2/ν_s instead of an 'imposed' timescale like ω^{-1}.

In the present work, we consider the influence of both *Pe* and *Sc* (or, *Wi* and *De*) numbers. As indicated above, it is usual in the analysis of start-up of steady shear-like flows to assume that $Sc = \infty$, and examine the transient and steady-state behaviour of the fluid for various *Pe* (or *Wi*) values. Thus, an important aspect of the present work is to examine the sensitivity of the solution to finite *Sc* (or *De*) numbers, including a determination of the lower bound on the range of values of *Sc* where the approximation $Sc = \infty$ can be used. Before turning to results, however, we discuss various aspects of the solution procedure in the next section.

3. Discussion of solution procedures

3.1. *The discretized form of the coordinate map*

In this section, we begin with a detailed discussion of the solution of (1.3) to obtain a discretized form of the coordinate map from reference to deformed configurations. Configuration space for a rigid orientable particle consists of the sphere of orientations. Thus the coordinate map is a map from the sphere of orientations in the reference configuration to the sphere of orientations in the deformed configuration. Since we consider a map from the sphere to the sphere, it would seem natural to use spherical polar coordinates. However, spherical polar coordinates lead in this case to major numerical difficulties associated with the singularity of the coordinate system, as we describe in Appendix A.

Rather than a spherical polar coordinate system, it is more practical to use local Cartesian coordinates (ξ, ψ, ζ) to describe the sphere of orientations, as shown in figure 1. Thus, we express the vector $\boldsymbol{R}$ in component form as

$$\boldsymbol{R}(t; \boldsymbol{R}_0) = \begin{pmatrix} \xi(t; \xi_0, \psi_0, \zeta_0) \\ \psi(t; \xi_0, \psi_0, \zeta_0) \\ \zeta(t; \xi_0, \psi_0, \zeta_0) \end{pmatrix}.$$

We emphasize that the local Cartesian coordinates (ξ, ψ, ζ) associated with each material point are distinct from (but parallel to) the global Cartesian coordinates (x, y, z). Moreover, (ξ_0, ψ_0, ζ_0) are local Cartesian coordinates associated with the reference configuration of a specific material point of suspension, and (ξ, ψ, ζ) are the local Cartesian coordinates associated with the current configuration of the same material point. As these coordinates describe points on the surface of the sphere, we put $\xi^2+\psi^2+\zeta^2 = 1$. The dimensionless evolution equations for the coordinate map $(\xi_0, \psi_0, \zeta_0) \rightarrow (\xi, \psi, \zeta)$ are (for a parallel flow $\boldsymbol{u} = u(y, t)\, \boldsymbol{e}_x$)

$$\frac{\partial \xi}{\partial t^*} = \frac{1}{2}\frac{\partial u^*}{\partial y^*}\psi + G\frac{1}{2}\frac{\partial u^*}{\partial y^*}\psi(1-2\xi^2) + \frac{1}{Pe}F^b_\xi, \tag{3.1a}$$

$$\frac{\partial \psi}{\partial t^*} = -\frac{1}{2}\frac{\partial u^*}{\partial y^*}\xi + G\frac{1}{2}\frac{\partial u^*}{\partial y^*}\xi(1-2\psi^2) + \frac{1}{Pe}F^b_\psi, \tag{3.1b}$$

$$\zeta = \pm(1-\xi^2-\psi^2)^{\frac{1}{2}}, \tag{3.1c}$$

where $\boldsymbol{F}^b = \boldsymbol{e}_\xi F^b_\xi + \boldsymbol{e}_\psi F^b_\psi + \boldsymbol{e}_\zeta F^b_\zeta$ is the Brownian term that we consider shortly. It may be observed that a (local) Cartesian coordinate representation of the sphere of orientations leads to evolution equations for the coordinate maps that avoid the problems associated with a singular coordinate system (see Appendix A). We have delayed an explicit representation of the Brownian force because it is accounted for in a geometrically motivated fashion. We return to this point shortly.

3.1.1. *Discretization of the sphere of orientations*

The contribution of the particles is accounted for as follows. At each of the $(K+1)$ material points $\{y^*_k, k = 0, \ldots, K\}$ across the half-thickness of the fluid layer, we compute the shear stress via (2.7). This calculation requires knowledge of the coordinate map between reference and deformed configurations, which is the solution of (3.1). Note that it is only necessary to solve (3.1) over the quarter-sphere

of orientations $\{(\sigma, \theta): 0 \leqslant \sigma \leqslant \pi, 0 \leqslant \theta \leqslant \frac{1}{2}\pi\}$, owing to symmetry considerations. (Although we solve for the coordinate map in Cartesian coordinates, it is at times convenient to refer to an equivalent (modified) spherical polar description, defined in figure 1.) In order to compute the coordinate map at each y_k^*, we follow the evolution of a set of particles with initial orientations

$$\left\{\left(\sigma_i = \frac{i\pi}{2j}, \theta_j = \frac{\pi}{2}\left(1 - \frac{j}{j_{max}}\right)\right): \quad 0 \leqslant i \leqslant 2j, \quad 0 \leqslant j \leqslant j_{max}\right\}. \tag{3.2}$$

This scheme for the discretization of the quarter-sphere of orientations has the advantage that the density of points in the grid per unit surface area is approximately constant. As an example, a value of $j_{max} = 10$ yields a discretization in which 121 points cover the quarter-sphere. If instead we used a 'regular grid' in (σ, θ) with the same resolution in the plane $\theta = 0$, we would require 211 points to cover the quarter-sphere, with an uneven distribution concentrated near $\theta = \frac{1}{2}\pi$. As one anticipates no dynamics of peculiar subtlety near $\theta = \frac{1}{2}\pi$, the increased discretization of a 'regular grid' would be wasted there.

3.1.2. *The Brownian term*

Now, we turn to the calculation of the Brownian term in (1.3). Rather than using a differential form of the Brownian term, we use a *geometrically motivated* form that we now describe. The grid (3.2) can be interpreted as defining an array of spherical triangles on the surface of the (quarter-) sphere of orientations, as indicated in figure 2. In pursuing a method for calculation of the Brownian term, we shall approximate the determinant of the deformation gradient tensor, $\det[\nabla_0 \boldsymbol{R}(t; \boldsymbol{R}_0)]$, as a (time-dependent) constant over each of the small spherical triangles defined by the grid (3.2), as it evolves in time. It is a simple matter to show that the expression $\det[\nabla_0 \boldsymbol{R}(t; \boldsymbol{R}_0)]$, integrated over one such spherical triangle in the reference configuration, gives the ratio of the areas of the same spherical triangle in the deformed to the reference configurations. Therefore, we can obtain the determinant of the deformation gradient tensor for each spherical triangle in the set that covers the quarter-sphere simply by computing the proper area ratios of spherical triangles.

With the approximation that $\det[\nabla_0 \boldsymbol{R}(t; \boldsymbol{R}_0)]$ is a constant over each spherical triangle in the grid, we have the following restatement of (1.2) in a form that is more suitable for numerical work:

$$f^*(t; \Delta_m) = \frac{1}{4\pi} \frac{\text{Area}[\Delta_m^0]}{\text{Area}[\Delta_m]},$$

where Δ_m symbolizes the mth spherical triangle in the deformed (current) configuration, and Δ_m^0 is the mth spherical triangle in the reference configuration. Thus the Brownian term, the last term in (1.3), may be written

$$\boldsymbol{F}^b = -\frac{\text{Area}[\Delta_m]}{\text{Area}[\Delta_m^0]} \nabla \left\{\frac{\text{Area}[\Delta_m^0]}{\text{Area}[\Delta_m]}\right\}. \tag{3.3}$$

The gradient in (3.3) is calculated by second-order-accurate finite differences on a grid with points at the centroid of each spherical triangle of which the particle in question is a vertex. In practice, this calculation is most efficiently performed on the plane tangent to the sphere of orientations at the point of interest, as sketched in figure 3. The triangles are not projected flat for the purpose of computing areas; only the locations

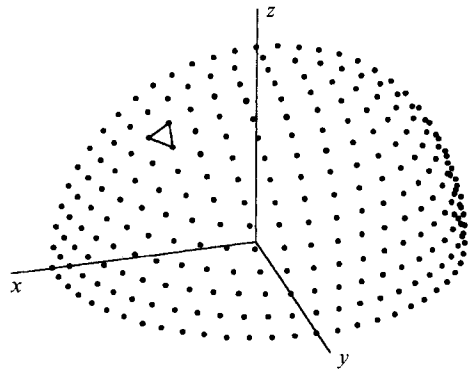

FIGURE 2. An example of the grid of orientations used to describe the coordinate map from reference to deformed configurations, showing the reference configuration for $j_{max} = 15$, together with one of the associated spherical triangles.

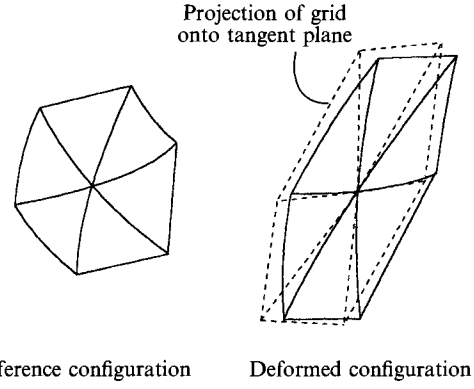

FIGURE 3. A sketch of the grid on which the Brownian term is evaluated using finite differences. The grid lies in the tangent plane of the sphere at the point of interest.

of the centroids are projected onto the tangent plane in order to facilitate computation of the gradient. If the triangles become highly deformed, this approximation may be a source of errors. This procedure is a stable and robust way to compute the highly nonlinear Brownian terms.

3.2. *Diagnostic quantities*

In summary, the parameters that we can vary in this example flow are:

(i) r, the aspect ratio of the particles, which fixes $\mu_i/\eta_s (i = 0, 1, 2, 3)$,
(ii) ϕ, the volume fraction of particles,
(iii) Pe, the Péclet number (alternatively this may be denoted as the Weissenberg number), and
(iv) Sc, the Schmidt number (alternatively, this may be denoted as the Deborah number).

For pressure-driven flows, the interesting quantity to measure is the flow rate acquired by the suspension in response to the applied pressure gradient. The dimensionless flow rate is

$$Q^* = \frac{Q}{hu_{cl}} 2 \int_0^1 u^* \, \mathrm{d}y^*.$$

If the flow is steady and Newtonian (Poiseuille flow), then the dimensionless flow rate for the suspending fluid (viscosity η_s) is $Q^*_{Newt} = \frac{4}{3}$ and the centreline velocity is related to the pressure drop in the channel as

$$u_{cl} = \frac{h^2}{2\eta_s}\frac{\partial p}{\partial x}. \tag{3.4}$$

For the non-Newtonian suspension flow, the only dimensionless group that depends on the flow rate is the Péclet number which is defined in terms of the Newtonian value for u_{cl}, see (2.10). Effectively, we use u_{cl} to represent the magnitude of the streamwise pressure gradient, and the Péclet number could equally well be defined in terms of the externally applied pressure gradient, $-\partial p/\partial x = G$, as

$$Pe = \frac{hG}{2D_R\eta_s}. \tag{3.5}$$

Thus, varying the Péclet number is equivalent to varying the applied pressure gradient. Of course, for the suspension the dimensionless volume flow rate for a given pressure drop will generally depend on all of the dimensionless parameters listed above, and will be smaller than the Newtonian value $Q^* = \frac{4}{3}$ for the suspending fluid.

3.3. *Solution strategy*

We solve the balance of linear momentum (2.3) using a finite difference method. For the Newtonian part of (2.3*a*), we use centred-space and backward-time differences to yield an implicit tridiagonal system that is solved by the Thomas algorithm. The grid includes $(K+1)$ points y^*_k across the half-thickness of the flow $0 \leqslant y^* \leqslant 1$ at which we compute the velocity. The particle contribution to the stress is left as a body force for the purposes of solution of (2.3).

The divergence of the particle contribution to the stress is computed as follows. At each grid point in the physical domain y^*_k, the particle contribution to the stress is computed by the methods we have outlined above. The derivative with respect to y^* is computed on this grid by second-order-accurate finite differences. No special particle dynamics are assumed to occur near the walls at $y^* = \pm 1$, for two reasons. First, it is not possible to regard the orientation of particles at the wall as a boundary condition on, say $\langle \boldsymbol{RR} \rangle$, because we do not solve a field equation for $\langle \boldsymbol{RR} \rangle$. Second, a recent study of dynamics of single particles in the neighbourhood of a wall (Dingman 1992) shows the wall to have very little effect on the motion of rod-like particles.

The order of solution of the equations is as follows. Let us assume that we know everything at a given time step and we wish to compute data at the next time step. We begin with the implicit solution of the momentum equation (2.6), where the non-Newtonian contribution to the stress is taken to be the value at the previous time step. Next, we use a predictor-corrector scheme to update the ensembles of orientations (3.2) that serve to define the discretized coordinate map at each material point y^*_k. The Brownian term is computed by finite difference approximation of (3.3). A new value for the non-Newtonian contribution of the stress is obtained, and then the velocity field is corrected.

4. Inhomogeneous pressure-driven flow

We turn to the results of our calculations of pressure-driven flows of a suspension of rigid orientable particles between parallel plates. Of course, steady pressure-driven

flow of a Newtonian fluid between parallel plates is simply Poiseuille flow; this is the baseline to which we compare.

4.1. *The start-up problem for different flow rates, and fixed Schmidt number*

Owing to the large number of parameters in the problem, we must work with a reduced set of values that yield interesting behaviour. In order to compare with the work of others (e.g. Hinch & Leal 1976), we consider suspensions of particles with a single, fixed aspect ratio $r = 5$. For the volume concentration ϕ, we choose 4 % which is roughly the upper limit of the dilute regime $\phi r^2 = O(1)$. The remaining two parameters are Péclet number and Schmidt number. In the following two sections we explore the influence of each of these separately, beginning with variation of Pe for fixed Sc. We have noted previously that the Péclet (or Weissenberg) number provides a measure of the expected degree of anisotropy, while Schmidt (or Deborah) number determines the significance of 'memory' effects with the limit $Sc = \infty$ representing the case of instantaneous response of the suspending fluid compared to the relaxation timescale of the suspension (i.e. D_R^{-1}). In the present section, we fix Schmidt number at $Sc = 10$. For this value of the Schmidt number, we have found that Pe between 0.5 and 100 encompasses most of the range of interesting behaviour. For example, for $Pe < 0.5$, we shall see that the orientation distribution near the walls, where the shear rate is largest, is virtually isotropic at steady state. On the other hand, for $Pe > 100$, it is virtually a delta function. Of course, for other values of Sc, the range of interesting values for Pe will be shifted one way or the other. Finally, it may also be noted (and shown in detail in the next section) that $Sc = 10$ is sufficiently large to approximate the limiting case $Sc = \infty$. Thus, the suspension response at each point should be very similar to the known behaviour of a dilute solution in a simple shear flow at the local shear rate (under the usual assumption that the suspending fluid flow is established instantaneously). Any differences are due to the fact that the concentration here is large enough that there is a moderate change in the flow due to the changes in the particle configuration, and this is not true in the usual studies of dilute suspension behaviour (cf. Hinch & Leal 1973; Advani & Tucker 1987, 1990; Altan, Advani & Güçeri 1989, among others).

Let us then consider briefly the computed results for fixed $Sc = 10$. The most obvious consequence of the addition of suspended particles, is that the suspension flows at a reduced rate compared to the pure (Newtonian) solvent when forced by the same pressure gradient. In figure 4 we plot the asymptotic steady normalized flow rate of the suspension, Q^*/Q^*_{Newt}, versus the logarithm of Pe. These solutions were obtained by integrating the start-up problem with initially isotropic particle distributions until a steady state was achieved. In addition to the reduced rate of flow of the suspension compared to that of a pure Newtonian fluid, one observes that the suspension exhibits shear-thinning behaviour; as the Péclet number increases, the flow rate of the suspension is closer to that of the pure Newtonian suspending fluid. The normalized volume flow rate levels off at low Péclet numbers to a plateau value which corresponds to a Newtonian fluid with a viscosity $\eta_{eff}/\eta_s = 1.232$, equal to that of the suspension with an isotropic orientation distribution everywhere in the domain. As the flow rate increases, the orientation distribution becomes increasingly anisotropic, beginning with the region near the walls, and the apparent viscosity decreases, reflecting a reduction in the effective viscosity near the walls. The upper limiting value of Q^*/Q^*_{Newt} at very large Pe corresponds to a constant viscosity fluid with viscosity, $\eta_{eff}/\eta_s = 1.113$ (cf. Hinch & Leal 1976) which is the value for maximal alignment of particles in the flow direction everywhere in the flow domain. At $Pe = 100$, the suspension exhibits its

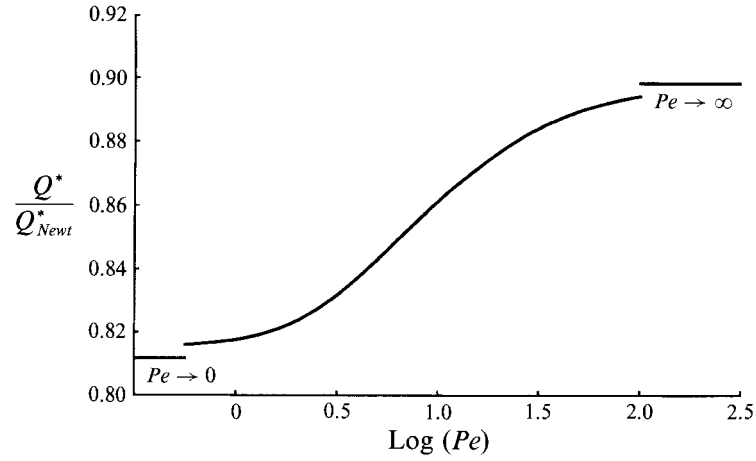

FIGURE 4. Normalized asymptotic flow rate of a pressure-driven flow of a suspension Q^*/Q^*_{Newt} versus the Péclet number Pe. Flows were computed for a suspension of particles of aspect ratio 5, volume concentration 4%, and Schmidt number $Sc = 10$. Note the shear-thinning behaviour exhibited over two magnitudes of Pe. The asymptotes for $Pe \to 0$ and $Pe \to \infty$ are shown.

asymptotic limiting behaviour over the majority of the flow domain but, as we shall see below, is still far from the high-Pe limiting behaviour in the immediate vicinity of the centreline.

This shear-thinning behaviour of the suspension is especially evident if one examines the asymptotic steady profiles of the effective shear viscosity (defined below) across the flow channel, shown in figure 5. The different curves in the figure correspond to the steady profiles of effective shear viscosity for different values of Pe. Of course, the effective shear viscosity, defined by

$$\left[\frac{\eta_{eff}}{\eta_s}\right](y^*, t^*) = \frac{\tau^{s*}_{xy} + \tau^{p*}_{xy}}{\partial u^*/\partial y^*}, \tag{4.1}$$

is not defined on the centreline, where the velocity gradient is zero. Thus, the curves $[\eta_{eff}/\eta_s](y^*, t \to \infty)$ shown in figure 5 do not begin at $y^* = 0$. It is obvious that the effective shear viscosity near the centreline must always be larger than that near the wall. What is interesting about the results in figure 5 is the sensitivity to Pe, and the fact that the effective viscosity approaches its large-Pe asymptotic value over such a large fraction of the flow domain at the relatively modest value of $Pe = 100$.

The cause of the drop in effective shear viscosity near the wall is, of course, the anisotropic contribution to the shear stress as a consequence of preferential orientation of particles by the flow. As there is no velocity gradient at the centreline, the orientation distribution of particles there is isotropic at all flow rates. The largest velocity gradients are near the wall; in steady Newtonian flow (Poiseuille flow), the magnitude of the (dimensionless) velocity gradient ranges from 0 on the plane of symmetry to 2 at the wall (i.e. the local Péclet or Weissenberg number varies from twice the characteristic value based on u_{cl}/h to 0 as we move from the wall to the channel centreline). This, in turn, leads to more anisotropic orientation distributions for particles near the wall.

In figure 6(a–c), we show snapshots of the particles at a specific material point near the wall for three different Péclet numbers: $Pe = 1$, 10 and 100, respectively. For reference, we also show an isotropic distribution of orientations, such as that of the ensemble on the centreline, in figure 6(d). There is a clear increase in the degree of

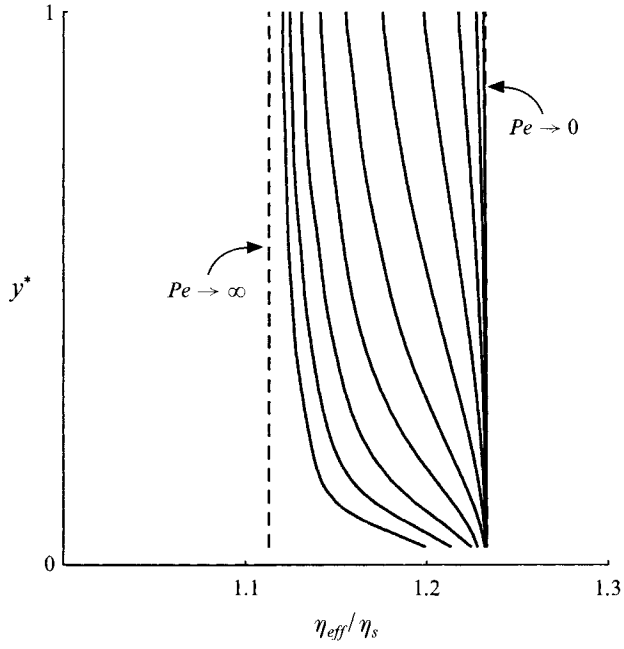

FIGURE 5. Asymptotic profiles of the local effective shear viscosity through the half-thickness of the flow. The contribution of the solvent is unity. These profiles correspond to the flows of figure 5, with Péclet numbers Pe = 100, 56.234, 31.623, 17.783, 10, 5.623, 3.162, 1.778, 1, 0.562, reading from left to right. The drop in local effective shear viscosity near the wall is most dramatic for the fastest flows. The left-most curve is associated with greatest anisotropy, whereas the right-most curve is associated with an almost isotropic suspension. The vertical dashed lines show the asymptotic values for $Pe \to \infty$ and $Pe \to 0$.

anisotropy with increased flow rate (hence greater Pe). Moreover, the dominant orientation of particles lies closer to the flow direction for higher flow rates, cf. figure 6(*a*, *c*). An obvious advantage of the double-Lagrangian technique over a technique such as direct solution of moment evolution equations is the capability to examine particle motions directly, in order to determine at the most basic level the source of observed non-Newtonian effects. Of course, knowledge of the components of the relevant moment tensor(s) (perhaps obtained through a standard approach with a closure model) does allow one to deduce dominant orientations of particles, etc. However, as we shall demonstrate shortly, some closure models in widespread use lead to non-physical values for the components of the moment tensor, even in uniform shear flow.

Finally, we examine the temporal evolution of the effective shear viscosity. The best way to understand the development of this spatially inhomogeneous flow is as follows. At each value of y^*, one can imagine conducting an (unsteady) uniform shear experiment in which anisotropy in particle orientation develops owing to the local velocity gradient. The asymptotic extent of anisotropy in the orientation distribution depends on the local velocity gradient $\dot{\gamma}$, just as it does in uniform shear flow. Moreover, in uniform shear flow, anisotropy of the particle orientation distribution evolves on the timescale $\dot{\gamma}t = O(Pe)$; hence, at different points in y^*, the flow is at a different stage of evolution, eventually merging as $t \to \infty$.

Initially the distribution of orientations is random; particles are set into motion along virtually undisturbed 'Jeffery' orbits characterized by trajectories that linger in

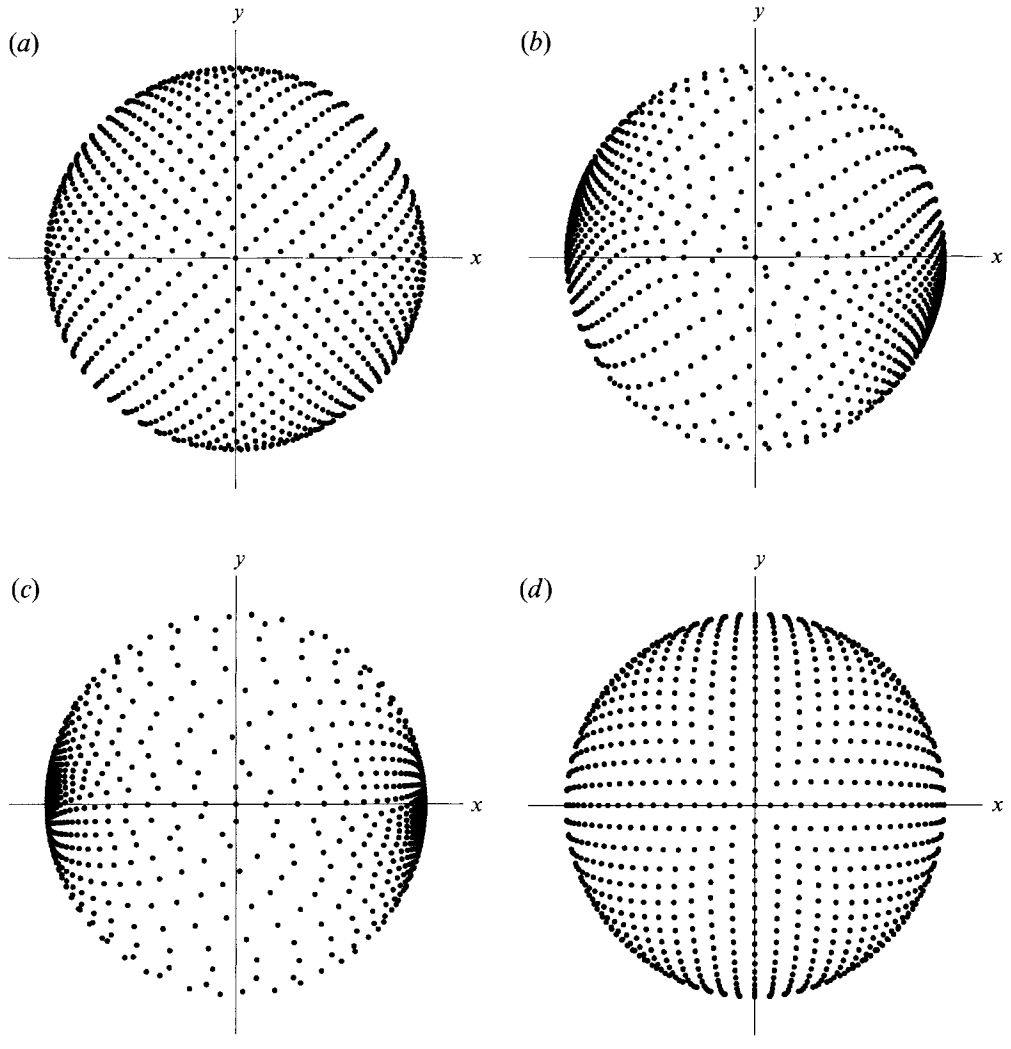

FIGURE 6. Instantaneous snapshot of the orientations of particles in an ensemble near the wall, in the asymptotically steady flow. Individual particle orientations are indicated by a dot ($z \geqslant 0$) on the sphere of orientations. (*a*) $Pe = 1$. Note the favoured orientation at about 25° clockwise from the x-axis. (*b*) $Pe = 10$. Anisotropy is increased, and the favoured orientation lies closer to the direction of flow. (*c*) $Pe = 100$. Anisotropy is still more extreme, and the favoured orientation lies even closer to the direction of flow. (*d*) Isotropic distribution of orientations, included for reference. This distribution is maintained at all times on the plane of symmetry of the pressure-driven flow.

a state approximately aligned with the flow, and then overturn. As is well known, the shear viscosity associated with particle motion along undisturbed Jeffery orbits is initially periodic in time in steady shear because the periodic rotation of the particles causes the orientation distribution function to be a periodic function if the initial distribution is random. However, in competition with this effect are the Brownian motions, which tend to redistribute particles both along and across the Jeffery orbits. This leads to a damping of the otherwise periodic shear viscosity. In shear flow, the damping is strong when the Péclet number is small so that Brownian motion is dominant over flow-induced particle orientation, and weak when it is large. The final steady-state viscosity (and the Eulerian form of the orientation distribution) is time

independent, even though individual particles continue to rotate periodically in time. (It may be noted however, that both the Lagrangian form of the distribution and the mapping on which it is based remain time dependent because the particles keep rotating.) We refer the reader to Leal & Hinch (1972) and Hinch & Leal (1973) for a discussion of these phenomena in various limiting cases. In the present flow, the situation is complicated by the fact noted earlier that the local Péclet number (based on the local shear rate) varies from approximately twice the nominal Péclet number (Pe) at the wall to zero at the plane of symmetry. Hence the microstructure, and therefore also the effective shear viscosity, evolves in a spatially inhomogeneous manner.

These points are illustrated in figure 7(*a–c*), in which we show the temporal evolution of the effective shear viscosity profiles when $Pe = 1$, 10 and 100 and $Sc = 10$. In figure 7(*a*) we show the development of the effective shear viscosity profile $[\eta_{eff}/\eta_s](y^*, t^*)$ for various t^* in the case of slow flow with $Pe = 1$. One observes that the shear viscosity near the wall overshoots slightly. Note that the oscillations about the asymptotic profile are very quickly damped in this case, achieving a steady state when $t^* = O(Sc)$.

When the flow rate is increased so that $Pe = 10$, the development of the effective shear viscosity profile is considerably more dynamic, as shown in figure 7(*b*). The effective shear viscosity increases throughout the layer, initially, and then drops near the wall to its asymptotic value. Near the plane of symmetry, where the local Péclet number is close to zero, note that there is no oscillation about the asymptotic value of the effective shear viscosity. Again, one observes that steady state is reached when $t^* = O(Sc)$.

In figure 7(*c*), in which we show $[\eta_{eff}/\eta_s](y^*, t^*)$ for various t^* and $Pe = 100$, the effect is even more dramatic. The effective shear viscosity overshoots, dropping to a wall value less than the asymptotic value of $[\eta_{eff}/\eta_s]$ near the walls. This is an indication that, instantaneously, the particle orientation distribution is more aligned with the flow than it is asymptotically. The evolving profile changes direction, with the shear viscosity growing near the wall, and overshoots the asymptotic profile once again. Finally, a steady state is achieved when $t^* = O(Sc)$. As before, however, the effective shear viscosity grows in a monotonic fashion near the plane of symmetry.

The data of figure 7(*c*) reflect, at least qualitatively, the transient behaviour that is observed for the suspension upon start-up of simple shear flow at increasing values of Pe (or Weissenberg number). It is well known in the latter case that the transient behaviour is monotonic in time for small Pe, but exhibits overshoots and an oscillatory approach to steady state that becomes increasingly pronounced as Pe is increased. We should emphasize here that all of the transient behaviour evident in figure 7 is due to the transient response of the orientation distribution to an instantaneously established shear flow of the suspending fluid. As we shall see in the next section, transients for smaller Schmidt (or Deborah) numbers will also reflect the evolution of the suspending fluid velocity profile on a finite timescale. The data of figure 7(*c*) demonstrate how waves arise naturally from the microscale physics, owing to the different rates of evolution of particle orientation distribution at different y^*. It is of interest to note, in the present context, that the differential equation for the velocity field (2.6) is parabolic, and so would not normally give rise to wave-like solutions. However, the complex interactions between macroscale and microscale evidently result in these phenomena which one normally associates with (explicitly) hyperbolic systems.

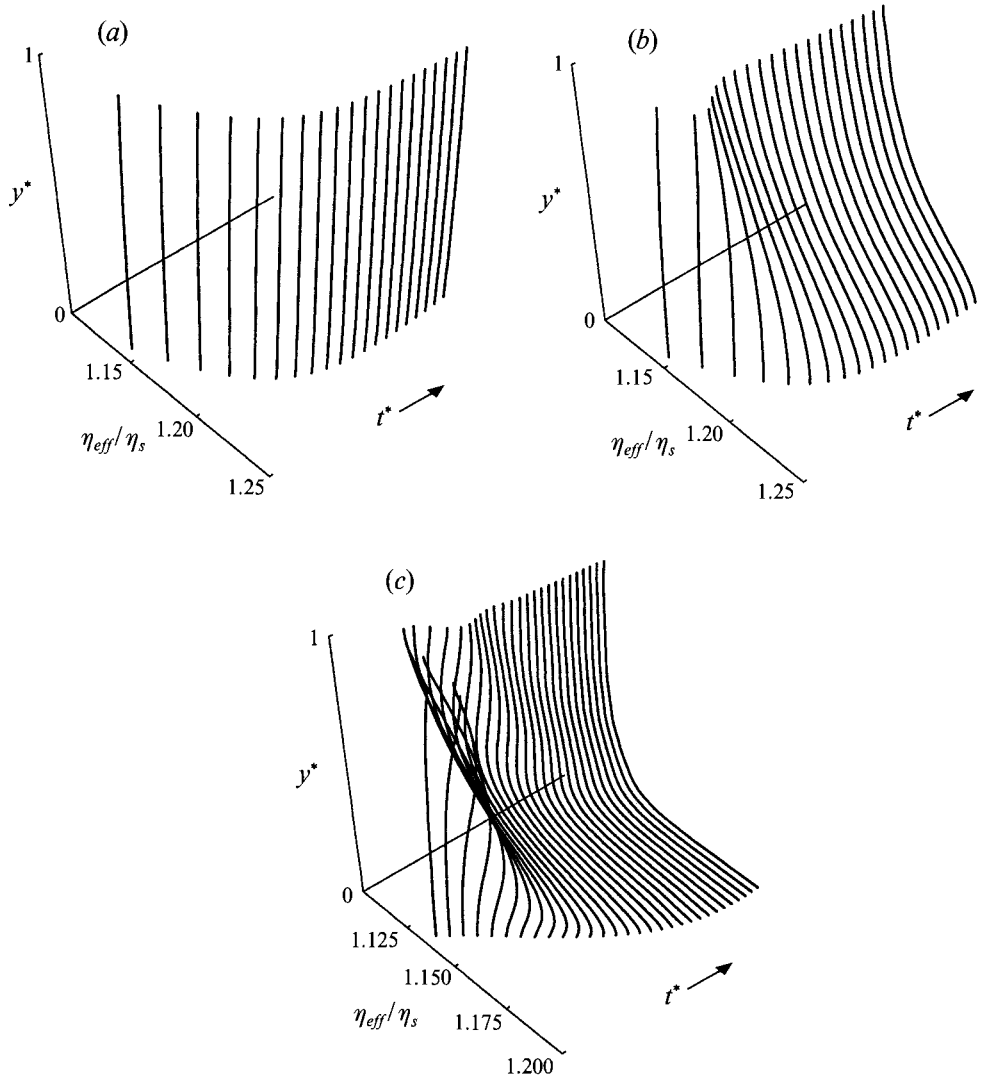

FIGURE 7. Transient local effective shear viscosity profiles. (*a*) $Pe = 1$. The times for the curves are $t^* = 0.5, 1.0, 1.5, \ldots, 10$ reading from front to back. The local effective shear viscosity is first slightly greater near the wall, and then slightly less near the wall as anisotropy in particle orientations develops near the wall. (*b*) $Pe = 10$; the times are $t^* = 0.5, 1.0, \ldots, 10.0$, reading from front to back. (*c*) $Pe = 10$; the times are $t^* = 0.1, 0.2, \ldots, 3.0$, reading from front to back. The development of the profile is extremely complicated, requiring several oscillations before settling down to steady state.

4.2. *The start-up problem for different Schmidt (Deborah) numbers*

As we pointed out previously, the Schmidt (or Deborah) number is the ratio of timescales for development of the orientation distribution of particles to the timescale for development of the Newtonian part of the flow. An interesting question arises if one contemplates an experimental study of pressure-driven flows of suspensions. A quite typical assumption in the analysis of experimental rheological data is that the velocity gradient seen by the particles is steady, i.e. develops instantaneously. Of course, all flows of Newtonian fluids require some finite time in which to become fully developed, and the question that arises quite naturally is: for a given suspension what is the

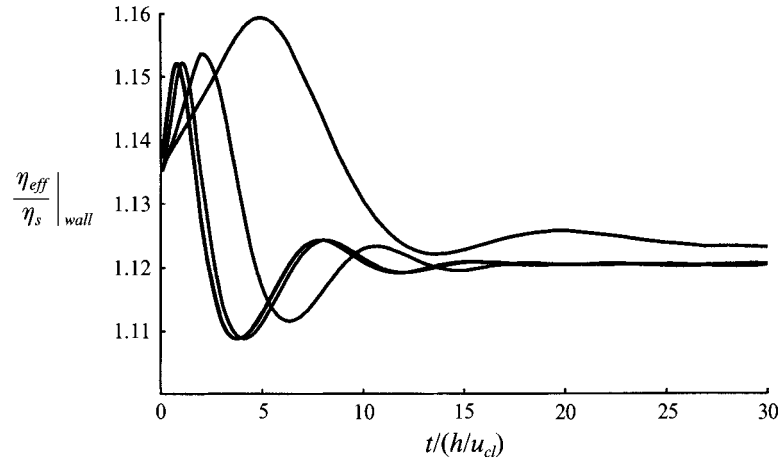

FIGURE 8. Effective shear viscosity at the wall versus time for the start-up of pressure-driven flow of a suspension with Schmidt number $Sc = \infty$, 1000 (virtually coincident), 100 (slight time lag) and 10 (considerable time lag), and 1 (major time lag). Each flow is computed with $Pe = 100$. This illustrates the point that the assumption of an instantaneously fully developed Newtonian part of the flow is valid for $Sc \gg 1$.

minimum value of the Schmidt number above which one can neglect the initial transient development of the Newtonian part of the flow field?

In order to address this question, we undertook the following numerical experiments. We set $Pe = 100$, and ran the start-up flow for Sc values of 1, 10, 1000 and ∞. The latter calculation corresponds to neglect of the initial transient in development of the Newtonian part of the flow. A plot of the effective shear viscosity at the wall versus $t(u_{cl}/h)$ for each Schmidt number is shown in figure 8. Although it is difficult to see, there are in fact five curves in the figure; the curves at $Sc = 1000$ and $Sc = \infty$ virtually coincide.

In figure 8, one observes immediately that the time traces for all $Sc \geqslant 10$ are qualitatively similar. However, there is a small time lag observable in the $Sc = 100$ curve, and a quite considerable lag when $Sc = 10$ (relatively to $Sc = \infty$). This supports our assertion that when $Sc \gg 1$, the Newtonian part of the flow develops sufficiently quickly, relative to the development of the particle orientation distribution, that the assumption of instantaneously fully developed Newtonian part of the flow is a good one.

The cases of $Sc = 1$ and 10 are seen to be quite different; this is clearly a consequence of the slow evolution of the Newtonian part of the flow field relative to the intrinsic timescale D_R^{-1}, for development of the orientation distribution. When the Newtonian part of the flow field evolves slowly, the particles near the wall experience a large magnitude of the velocity gradient for an important portion of the time over which the orientation distribution evolves. This increased value of the velocity gradient at the wall is responsible for the time-lag one observes for $Sc = 1$ and 10 in figure 8.

It may seem rather surprising at first that the criterion for neglect of the initial transient in the development of the velocity profile for the suspending fluid depends only on Sc, because it can be seen from the definition (2.9) that this means that the answer nas nothing to do with the nominal flow rate (i.e. the applied pressure gradient). The two competing timescales are the diffusive timescale h^2/ν_s and the natural relaxation timescale of the fluid, namely the inverse rotational Brownian diffusivity D_R^{-1}

(whose ratio is Sc), and neither depends in any way on the flow rate. Nevertheless, some care needs to be taken in the interpretation of this result. We assume implicitly for all of our calculations that the flow channel is sufficiently long that end effects can be completely neglected. In particular, the length of the entry region where the flow and the orientation distribution are developing must be small compared to the total length of the flow channel if the results obtained here are to have a direct counterpart in the macroscopic flow rate/pressure gradient data.

This criterion will be easiest to satisfy when the flow rate is lowest, because the distance travelled downstream from the entry to the fully developed region is directly proportional to u_{cl}, i.e.

$$L/h \text{ for steady state} \approx Pe, \qquad Sc \gg 1;$$
$$L/h \text{ for steady state} \approx Pe/Sc, \quad Sc \ll 1.$$

Thus, given a flow channel of some fixed length-to-width ratio, L/h, there will be a maximum flow rate above which the entry region cannot be ignored in the interpretation of experimental results. However, this is quite distinct, as indicated already, from neglect of the initial transient in the suspending fluid flow. Clearly, for the latter it is necessary that $Sc \geqslant 100$ or even 1000, depending upon the expected level of temporal resolution.

5. Evaluation of closure approximations

Now we compare the results of our calculations to those we obtain by direct solution of moment evolution equations derived using two different closure approximations. This comparison shows the closure approximations to be in error, but more importantly reveals that non-physical effects may be predicted by the closure models. These possibilities for non-physical behaviour in the closure models are investigated by consideration of the structure of the associated equations.

As discussed previously, the object of a closure approximation is to write a higher-order moment of the distribution function in terms of lower-order moments, in order that one may derive a closed set of evolution equations for the moment(s) required to calculate the stresses. One common approximation is the so-called quadratic approximation,

$$\langle \boldsymbol{RRRR} \rangle : \boldsymbol{E} \approx \langle \boldsymbol{RR} \rangle \langle \boldsymbol{RR} \rangle : \boldsymbol{E}, \tag{5.1a}$$

which is attractive primarily due to its simple form. A more sophisticated approximation is the composite closure derived by Hinch & Leal (1975, 1976),

$$\langle \boldsymbol{RRRR} \rangle : \boldsymbol{E} \approx \tfrac{1}{5}[6\langle \boldsymbol{RR} \rangle \cdot \boldsymbol{E} \cdot \langle \boldsymbol{RR} \rangle - \langle \boldsymbol{RR} \rangle \langle \boldsymbol{RR} \rangle : \boldsymbol{E} - 2\boldsymbol{I}\langle \boldsymbol{RR} \rangle^2 : \boldsymbol{E} + 2\boldsymbol{I}\langle \boldsymbol{RR} \rangle : \boldsymbol{E}]. \tag{5.1b}$$

The latter expression has the correct limiting form in weak and in strong flows. As discussed at some length in I, both approximations have been shown to result in errors, especially for suspensions of particles with large aspect ratio. We shall test these closure models against the results of the example calculations reported above, which span the range of Pe (or Wi) between the high- and low-shear-rate Newtonian regimes for a suspension of particles with aspect ratio 5, volume concentration 4% and $Sc = 10$. As erroneous behaviour is already well-known for the closure models for particles of large aspect ratio, our tests are therefore not the most demanding tests of the closure approximations that one might devise. Nevertheless, as we shall see, these approximations can lead to non-physical behaviour.

In the present case of unidirectional flow, the particle contribution to the stress for the quadratic closure is easily computed as

$$\tau_{xy}^{p} = \mu_0 \phi \frac{\partial u}{\partial y} + \mu_1 \phi D_R \langle RR \rangle_{xy} + \mu_2 \phi \frac{\partial u}{\partial y} \langle RR \rangle_{xy}^2 + \mu_3 \phi \frac{\partial u}{\partial y} [\langle RR \rangle_{xx} + \langle RR \rangle_{yy}], \quad (5.2)$$

and the moment evolution equations are, in components,

$$\frac{\mathrm{d}}{\mathrm{d}t} \langle RR \rangle_{xx} = 2D_R - 6D_R \langle RR \rangle_{xx} + \frac{\partial u}{\partial y}(1+G)\langle RR \rangle_{xy} - 2G \frac{\partial u}{\partial y} \langle RR \rangle_{xx} \langle RR \rangle_{xy}, \quad (5.3a)$$

$$\frac{\mathrm{d}}{\mathrm{d}t} \langle RR \rangle_{xy} = -6D_R \langle RR \rangle_{xy} + \frac{1}{2} \frac{\partial u}{\partial y}(-1+G)\langle RR \rangle_{xx} + \frac{1}{2} \frac{\partial u}{\partial y}(1+G)\langle RR \rangle_{yy} - 2G \frac{\partial u}{\partial y} \langle RR \rangle_{xy}^2, \quad (5.3b)$$

$$\frac{\mathrm{d}}{\mathrm{d}t} \langle RR \rangle_{yy} = 2D_R - 6D_R \langle RR \rangle_{yy} + \frac{\partial u}{\partial y}(-1+G)\langle RR \rangle_{xy} - 2G \frac{\partial u}{\partial y} \langle RR \rangle_{xy} \langle RR \rangle_{yy}. \quad (5.3c)$$

The evolution equations for the other components ($\langle RR \rangle_{xz}, \langle RR \rangle_{yz}, \langle RR \rangle_{zz}$) are not required for evaluation of the particle contribution to the stress.

For the composite closure approximation of Hinch & Leal, the particle contribution to the shear stress is

$$\tau_{xy}^{p} = \mu_0 \phi \frac{\partial u}{\partial y} + \mu_1 \phi D_R \langle RR \rangle_{xy} + \mu_2 \phi \frac{\partial u}{\partial y} \left[\frac{2}{5} \langle RR \rangle_{xy}^2 + \frac{3}{5} \langle RR \rangle_{xx} \langle RR \rangle_{yy} \right] + \mu_3 \phi \frac{\partial u}{\partial y} [\langle RR \rangle_{xx} + \langle RR \rangle_{yy}], \quad (5.4)$$

and the moment evolution equations are

$$\frac{\mathrm{d}}{\mathrm{d}t} \langle RR \rangle_{xx} = 2D_R - 6D_R \langle RR \rangle_{xx} + \frac{\partial u}{\partial y}\left(1 + \frac{G}{5}\right)\langle RR \rangle_{xy} - \frac{6}{5} G \frac{\partial u}{\partial y} \langle RR \rangle_{xx} \langle RR \rangle_{xy} + \frac{4}{5} G \frac{\partial u}{\partial y} \langle RR \rangle_{xy} \langle RR \rangle_{yy} + \frac{4}{5} G \frac{\partial u}{\partial y} \langle RR \rangle_{xz} \langle RR \rangle_{yz}, \quad (5.5a)$$

$$\frac{\mathrm{d}}{\mathrm{d}t} \langle RR \rangle_{xy} = -6D_R \langle RR \rangle_{xy} + \frac{1}{2} \frac{\partial u}{\partial y}(-1+G)\langle RR \rangle_{xx} + \frac{1}{2} \frac{\partial u}{\partial y}(1+G)\langle RR \rangle_{yy} - \frac{4}{5} G \frac{\partial u}{\partial y} \langle RR \rangle_{xy}^2 - \frac{6}{5} G \frac{\partial u}{\partial y} \langle RR \rangle_{xx} \langle RR \rangle_{yy}, \quad (5.5b)$$

$$\frac{\mathrm{d}}{\mathrm{d}t} \langle RR \rangle_{yy} = 2D_R - 6D_R \langle RR \rangle_{yy} + \frac{\partial u}{\partial y}\left(-1 + \frac{G}{5}\right)\langle RR \rangle_{xy} - \frac{6}{5} G \frac{\partial u}{\partial y} \langle RR \rangle_{xy} \langle RR \rangle_{yy} + \frac{4}{5} G \frac{\partial u}{\partial y} \langle RR \rangle_{xx} \langle RR \rangle_{xy} + \frac{4}{5} G \frac{\partial u}{\partial y} \langle RR \rangle_{xz} \langle RR \rangle_{yz}. \quad (5.5c)$$

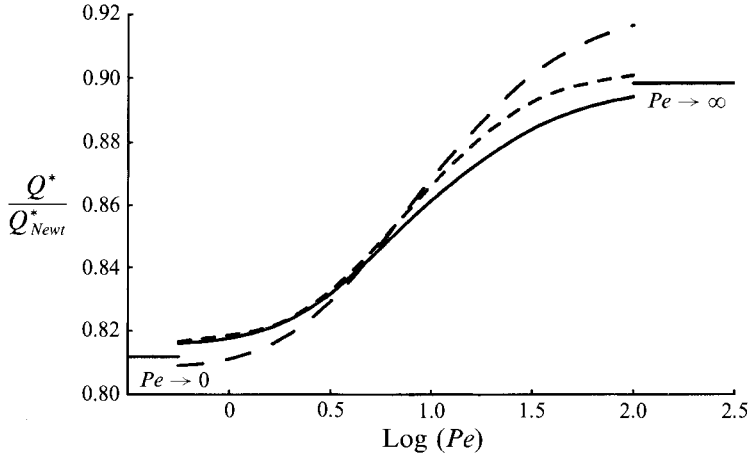

FIGURE 9. Comparison of the shear-thinning behaviour of the suspension, calculated using: the (exact) double-Lagrangian technique (——), using integration of direct moment evolution equations with the quadratic closure (– – –), and using the Hinch–Leal composite closure (----). These calculations are for a suspension of particles of aspect ratio 5, volume concentration 4%, and Schmidt number $Sc = 10$. The asymptotes for $Pe \to 0$ and $Pe \to \infty$ are shown.

Note that we generally also require the additional equations

$$\frac{\mathrm{d}}{\mathrm{d}t}\langle RR\rangle_{xz} = -6D_R\langle RR\rangle_{xz} + \frac{1}{2}\frac{\partial u}{\partial y}(1+G)\langle RR\rangle_{yz} - \frac{4}{5}G\frac{\partial u}{\partial y}\langle RR\rangle_{xy}\langle RR\rangle_{xz} - \frac{6}{5}G\frac{\partial u}{\partial y}\langle RR\rangle_{xx}\langle RR\rangle_{yz}, \quad (5.5d)$$

$$\frac{\mathrm{d}}{\mathrm{d}t}\langle RR\rangle_{yz} = -6D_R\langle RR\rangle_{yz} + \frac{1}{2}\frac{\partial u}{\partial y}(-1+G)\langle RR\rangle_{yz} - \frac{4}{5}G\frac{\partial u}{\partial y}\langle RR\rangle_{xy}\langle RR\rangle_{xz} - \frac{6}{5}G\frac{\partial u}{\partial y}\langle RR\rangle_{xz}\langle RR\rangle_{yy}. \quad (5.5e)$$

However, the initial conditions on $\langle RR\rangle_{xz}$ and $\langle RR\rangle_{yz}$ are zero for an isotropic initial state; hence (5.5*d*, *e*) lead to the conclusion that $\langle RR\rangle_{xz}$ and $\langle RR\rangle_{yz}$ are zero for all time. Thus we need to integrate (5.5*a–c*) only, in order to obtain the required moment components for the particle contribution to the shear stress.

5.1. *Pressure-driven flow computed using different closure models*

Now we compare the exact pressure-driven flow calculations that we have reported in the previous section, with the results one can obtain using the quadratic closure or the Hinch–Leal composite closure. In figure 9, we show the asymptotic, normalized flow rate plotted against the logarithm of Pe for the double-Lagrangian calculation (the full equations), for the pre-averaged closure, and for the Hinch–Leal closure. All three solutions show the shear-thinning effect, and, to some degree, the levelling-off at the transition to the two Newtonian regimes. The Hinch–Leal closure reflects the shear-thinning behaviour more accurately; the greatest departure from the exact results occurs for the largest Péclet numbers. Even so, the Hinch–Leal closure is accurate to within about 10% in predicting the deficit in flow rate due to the addition of particles for the full range of parameters that we investigated.

The quadratic closure is not as accurate, either for slow or for fast flows. It tends to yield shear-thinning behaviour that is considerably more dramatic than the full equations would suggest. At its worst, the pre-averaged closure is more than 30% in error in predicting the deficit in flow due to the addition of particles in the calculations reported here.

In figure 10(*a–c*), we compare asymptotic shear viscosity profiles obtained by the three methods at $Pe = 0.1$, 10, and 100, respectively. Figure 10(*a*) shows very accurate approximation by the Hinch–Leal closure, and an over-prediction of the shear viscosity by the pre-averaged closure. At $Pe = 10$, the profiles in figure 10(*b*) reveal that the closure approximations both tend to over-predict the shear-thinning behaviour of the suspension. The decrease in effective shear viscosity near the walls is larger for the quadratic closure and the Hinch–Leal closure than for the full equations. This effect is more evident in figure 10(*c*), where we show the effective shear viscosity profles when $Pe = 100$.

Figures 10(*c*) and 9 indicate that the principal problem with the pre-averaged closure is its failure to predict adequately the transition to the second Newtonian regime at high values of *Pe*. In figure 9, the long-dashed curve does not level off at high *Pe*, as do the curves corresponding to the Hinch–Leal closure and the full equations. In figure 10(*c*), the quadratic closure profile of the effective shear viscosity continues to drop near the wall while the profiles for the Hinch–Leal closure and for the full equations level off.

5.2. *Observed non-physical behaviour in closure models*

At this moderate value of the particle aspect ratio ($r = 5$), the closure approximations seem to perform adequately in capturing the qualitative shear-thinning behaviour of the suspension. However, there are pathological problems with the closure approximations that surfaced during the integration of the moment evolution equations. To be specific, we found that both closures can lead to non-physical components of the moment tensor, even in uniform shear flow. An example of this phenomenon is shown in figure 11(*a–c*), where we have plotted time traces (rescaled by the shear rate) of the moment components obtained from simulation of the full equations by our new technique (figure 11*a*), by integration of the quadratic closure equations (5.3) (figure 11*b*), and by integration of the Hinch–Leal composite closure equations (5.5) (figure 11*c*). This integration is carried out for a uniform shear flow with Péclet number defined by $Pe = (1/D_R)\,(\partial u/\partial y) = 200$.

Upon examination, the time traces in figures 11(*a*) and 11(*b*) look qualitatively similar; thus the quadratic closure equations have the same qualitative transient behaviour as the full equations. Figure 11(*c*), however, looks quite different. First, one notices that oscillations in the moments persist for a considerably longer time with the Hinch–Leal composite closure than with the pre-averaged closure or the full equations. This has to do, no doubt, with the nonlinear terms in the closure model equations. More importantly, the time trace of $\langle RR\rangle_{yy}$ in figure 6(*c*) shows that this diagonal component of the moment is negative over a significant period of time early in the response. This is, of course, non-physical, as it would correspond to negative probabilities of particle orientations in the associated direction.

5.3. *The source of non-physical behaviour in closure models*

This pathological behaviour is actually possible in both of the closure approximations that we have considered, as one may establish by the following arguments. Consider first the pre-averaged closure equations. Our goal is to investigate when negative values for the diagonal components $\langle RR\rangle_{xx}$ and $\langle RR\rangle_{yy}$ are possible. In this connection, it

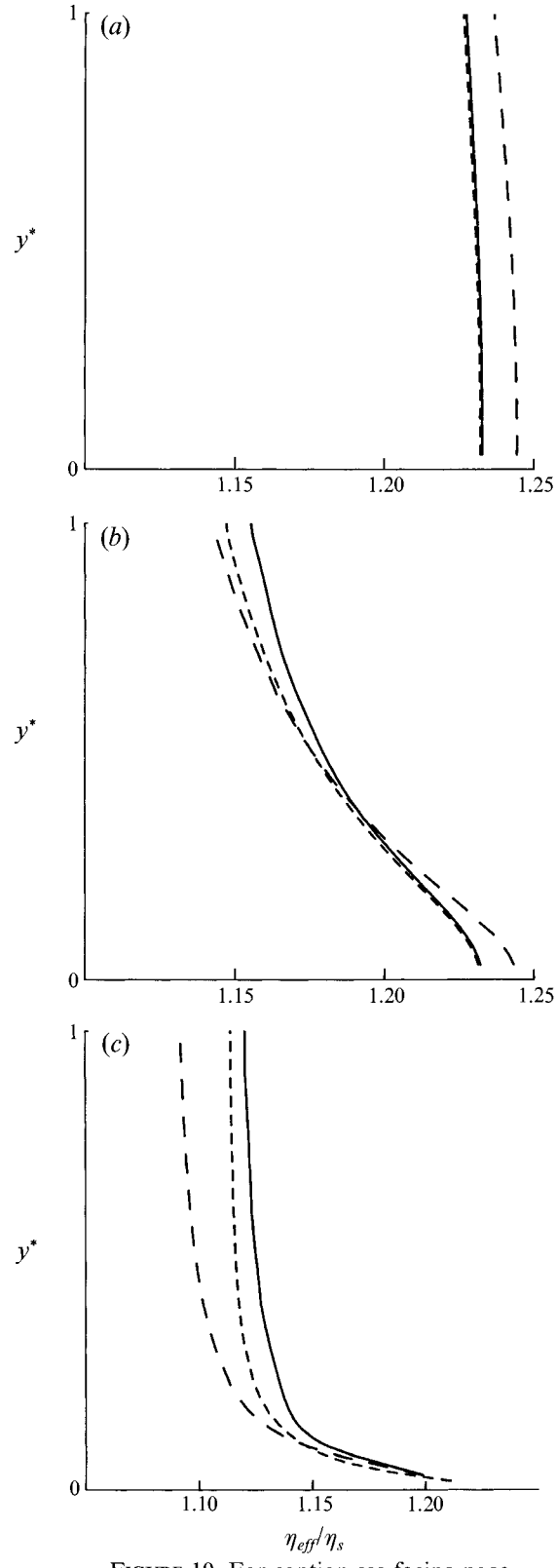

FIGURE 10. For caption see facing page.

is profitable to consider the three-dimensional phase space of equations (5.3) which has coordinates $\langle RR\rangle_{xx}$, $\langle RR\rangle_{yy}$, and $\langle RR\rangle_{xy}$. At the boundaries of the first quadrant of the $(\langle RR\rangle_{xx}, \langle RR\rangle_{yy})$-plane, we require that the vector field of (5.3) be directed inward, into the first quadrant. For only then will $\langle RR\rangle_{xx} \geqslant 0$ and $\langle RR\rangle_{yy} \geqslant 0$ be assured for all time, assuming this is true initially. Now we check (5.3) to see whether this is so. First we evaluate (5.3*a*) on the first quadrant boundary $\langle RR\rangle_{xx} = 0$

$$\frac{1}{D_R}\frac{\mathrm{d}}{\mathrm{d}t}\langle RR\rangle_{xx}\bigg|_{\langle RR\rangle_{xx}=0} = 2 + Pe(1+G)\langle RR\rangle_{xy}. \tag{5.6a}$$

Similarly, we evaluate (5.3*c*) on the first quadrant boundary $\langle RR\rangle_{yy} = 0$

$$\frac{1}{D_R}\frac{\mathrm{d}}{\mathrm{d}t}\langle RR\rangle_{yy}\bigg|_{\langle RR\rangle_{yy}=0} = 2 + Pe(-1+G)\langle RR\rangle_{xy}. \tag{5.6b}$$

Now, bearing in mind that the off-diagonal moment component $\langle RR\rangle_{xy}$ may be positive or negative at any instant, it is clear that (5.6) show that non-physical, negative moment components $\langle RR\rangle_{xx}$ and $\langle RR\rangle_{yy}$ may arise in quite general situations. One can argue from (5.6*a*) that the possibility of negative diagonal moment components is greater when the Péclet number is large, and when the particle aspect ratio (hence also G) is large.

These same arguments may be applied to the Hinch–Leal composite closure equations, with a similar conclusion. Equations (5.5*a*) and (5.5*c*) lead to

$$\frac{1}{D_R}\frac{\mathrm{d}}{\mathrm{d}t}\langle RR\rangle_{xx}\bigg|_{\langle RR\rangle_{xx}=0} = 2 + Pe\left(1+\frac{G}{5}\right)\langle RR\rangle_{xy} + \frac{4}{5}G\,Pe\langle RR\rangle_{xy}\langle RR\rangle_{yy}, \tag{5.7a}$$

$$\frac{1}{D_R}\frac{\mathrm{d}}{\mathrm{d}t}\langle RR\rangle_{yy}\bigg|_{\langle RR\rangle_{yy}=0} = 2 + Pe\left(-1+\frac{G}{5}\right)\langle RR\rangle_{xy} + \frac{4}{5}G\,Pe\langle RR\rangle_{xx}\langle RR\rangle_{xy}. \tag{5.7b}$$

In the worst instance, $\langle RR\rangle_{yy} = 1$ for (5.7*a*), and $\langle RR\rangle_{xx} = 1$ for (5.7*b*); thus the worst-case forms of (5.7) are (5.6)! The same arguments as for the quadratic equations lead to the conclusion that the Hinch–Leal composite closure equations may also develop negative diagonal moment components.

These considerations may prompt one to ask why are there negative diagonal moment components in figure 11(*c*) but not in figure 11(*b*), if both closures have the same possibility of pathological behaviour at high shear rates. The answer is that the arguments presented above apply to the whole of phase space, whereas the time traces of figure 11 represent a single solution with isotropic initial condition. It happens that the solution beginning at this isotropic initial condition leaves the first quadrant of the $(\langle RR\rangle_{xx}, \langle RR\rangle_{yy})$-plane for the Hinch–Leal closure equations, but not for the quadratic closure equations. Our analysis of the vector fields of these equations indicates that there are initial conditions (not necessarily isotropic) that lead to non-physical, negative diagonal moment components for both closures.

Of course, our results for the shear stresses obtained by the closure models are not too terrible, being from 10–30% inaccurate compared to the full equations for the examples we tested. However, if one uses the components of the moment tensors to

FIGURE 10. Comparison of the effective shear viscosity profiles. The different curves are calculated using the double Lagrangian technique (——), using integration of direct moment evolution equations with the quadratic closure (– – –), and using the Hinch–Leal composite closure (- - - -). (*a*) $Pe = 1$; (*b*) $Pe = 10$; (*c*) $Pe = 100$.

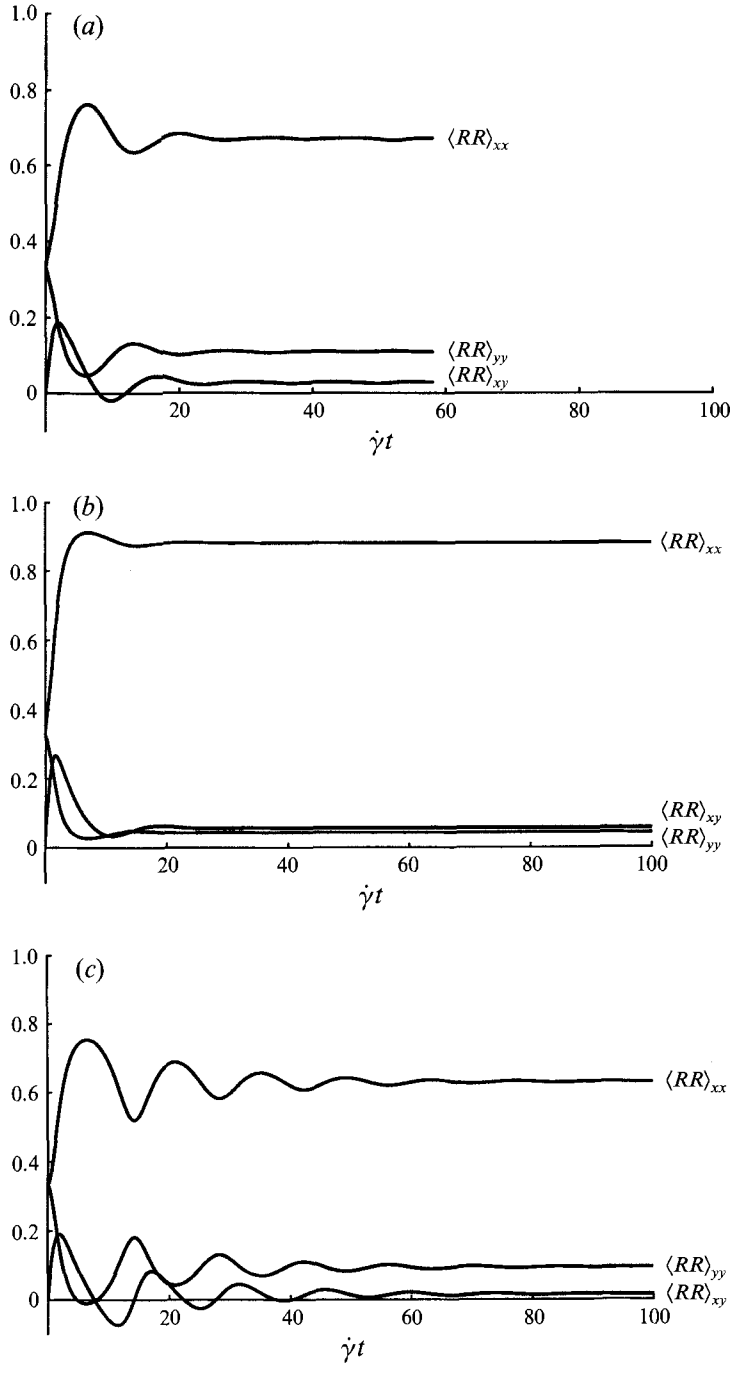

FIGURE 11. The moments $\langle RR\rangle_{xx}$, $\langle RR\rangle_{xy}$ and $\langle RR\rangle_{yy}$ *vs.* time multiplied by the shear rate for uniform shear flow at Péclet number 200, obtained by (*a*) the double-Lagrangian technique; (*b*) obtained by integration of direct moment evolution equations with the quadratic closure; (*c*) obtained by integration of direct moment evolution equations with the Hinch–Leal composite closure. Note the non-physical behaviour in (*c*) when the diagonal moment component $\langle RR\rangle_{yy}$ is negative.

deduce characteristics of the solution such as dominant particle orientations, etc., one will undoubtedly run into serious trouble when using these closure approximations. In addition, the transient behaviour of the full equations can be quite different from the transient behaviour of closure models, as shown in figure 11. This may lead to instabilities in numerical integration of closure models that have nothing whatever to do with the behaviour of solutions to the model equations without closure approximations.

5.4. *Manifestations of non-physical behaviour in prior work*

In the previous subsection, we argued that non-physical behaviour may arise in either closure model that we examined. While the closure models were found to be in error by 10–30% in their predictions of the shear-thinning behaviour of the suspension, the diagonal components of the second moment tensor were capable of becoming negative over a portion of their evolution when computed by the closure models.

This evaluation of closure models is not the first that has been undertaken. Advani & Tucker (1989) report an evaluation of closure models including the quadratic closure (5.1*a*). Their evaluation consists of integrating the moment evolution equations in a steady uniform flow and checking the result against the solution of the associated Fokker–Planck equation. However, the orientation distributions, like the flow fields, are assumed to be planar, and so this analysis is not directly related to the present work.

Similarly, the work of Altan *et al.* (1989) is not directly applicable, as these authors consider the case $D_R = 0$. They do, however, consider three-dimensional orientation distributions modelled by the quadratic closure, among others. They observed considerable quantitative discrepancies between closure models and their exact solutions.

The excellent paper of Frattini & Fuller (1986) is of greatest relevance to the present discussion. Their paper reports the results of careful uniform shear flow experiments conducted on two different suspensions, together with parallel numerical integrations of closure models under the same flow conditions. It is interesting to note that they report their results in terms of degree of alignment of the particles

$$\frac{\Delta n''}{\Delta n''_{max}} = [4\langle RR\rangle_{xy} + (\langle RR\rangle_{yy} - \langle RR\rangle_{xx})^2]^{\frac{1}{2}} \tag{5.8a}$$

and the (predominant) angle of orientation σ^*

$$\tan 2\sigma^* = \frac{2\langle RR\rangle_{xy}}{\langle RR\rangle_{xx} - \langle RR\rangle_{yy}}, \tag{5.8b}$$

rather than in terms of moment components. It is for this reason, we believe, that Frattini & Fuller appear to have overlooked the non-physical behaviour in the closure models to which we have earlier made reference.

In our investigation of the non-physical behaviour made possible by the closure approximations, we performed the calculations necessary to reproduce figures 15(*a*) and 16(*a*) of their paper. However, the time trace from the experiment in their figures is replaced by the exact solution of the microdynamical equations by the double-Lagrangian technique in our comparable figures 12(*a*) and 12(*b*). For the given conditions of $Pe = 187$ and aspect ratio of particles $r = 6.8$, it would appear that we have successfully reproduced their calculations; in fact, the double-Lagrangian trace in figures 12(*a*) and 12(*b*) is remarkably similar to the experimental result reported in

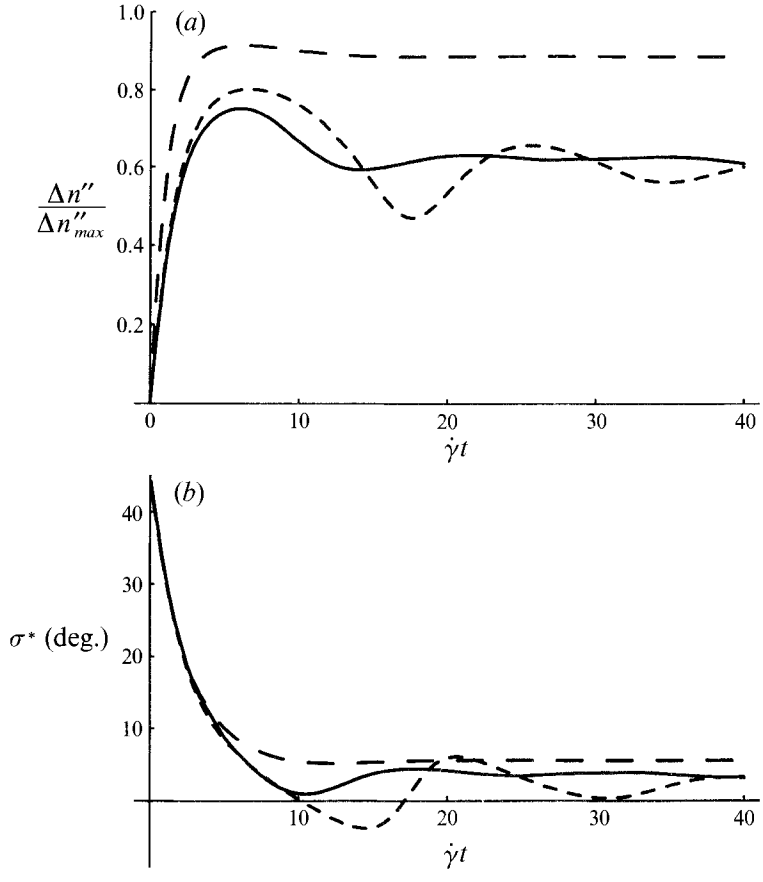

FIGURE 12. (*a*) Degree of alignment ($\Delta n''/\Delta n''_{max}$) of suspension of rod-like particles of aspect ratio $r = 6.8$ in uniform shear flow with $Pe = 187$; a reproduction of part of figure 15(*a*) of Frattini & Fuller (1986). The curves are calculated using the double Lagrangian technique (——), using integration of direct moment evolution equations with the quadratic closure (– – –), and using the Hinch–Leal composite closure (----). Note the extended transient behaviour of the Hinch–Leal closure. (*b*) Dominant orientation angle of particles, σ^*, relative to the direction of flow of a suspension of rod-like particles of aspect ratio $r = 6.8$ in uniform shear flow with $Pe = 187$; a reproduction of part of figure 16(*a*) of Frattini & Fuller (1986). The different results are calculated using the double Lagrangian technique (——), using integration of direct moment evolution equations with the quadratic closure (– – –), and using the Hinch–Leal composite closure (----). Note the overshoot in orientation angle of the Hinch–Leal closure.

figures 15(*a*) and 16(*a*) of Frattini & Fuller, especially considering the rather broad dispersion in aspect ratio of their experimental material.

Frattini & Fuller noted with interest the longer transient in the Hinch–Leal closure model, as well as the curious overshoot in orientation angle visible in figure 12(*b*). They explained both phenomena on the basis of an inaccurate account of Brownian effects at intermediate Péclet numbers. We offer here a complementary explanation: that the longer transient and overshoot in orientation angle are related to non-physical behaviour in the closure model. This can be observed in figure 13(*a–c*), in which we plot the moment traces corresponding to figure 12(*a*, *b*) for the exact solution by the double-Lagrangian technique, for the pre-averaged closure model, and for the Hinch–Leal closure model. Upon examination, one observes that the diagonal second moment component integrated by the Hinch–Leal closure, $\langle RR \rangle_{yy}$, is negative over

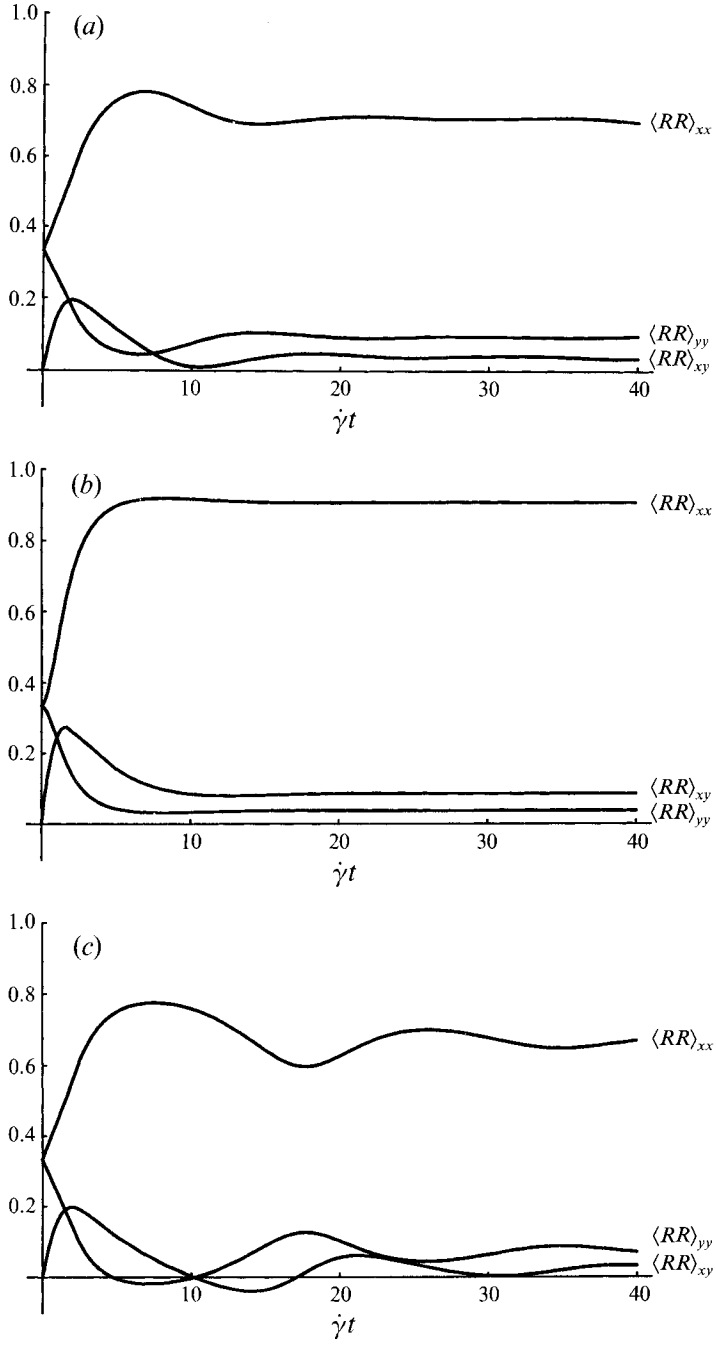

FIGURE 13. The moments $\langle RR\rangle_{xx}$, $\langle RR\rangle_{xy}$ and $\langle RR\rangle_{yy}$ *vs.* time multiplied by the shear rate, for uniform shear flow at Péclet number 187 of a suspension of rod-like particles with aspect ratio 6.8; (*a*) obtained by the double-Lagrangian technique; (*b*) obtained by the quadratic closure model; (*c*) obtained by the Hinch–Leal closure model. Note the non-physical negative diagonal component of the second moment tensor $\langle RR\rangle$ in (*c*).

the time interval $4.3 \leqslant \dot{\gamma}t \leqslant 10$. In figure 12(*b*) one observes that significant overshoot occurs in the orientation angle beginning at about $\dot{\gamma}t = 10$. It would appear that during integration by the Hinch–Leal closure, there is a strong 'kick' back to $\langle RR \rangle_{yy} > 0$ at $\dot{\gamma}t = 10$, and that this kick results in an overshoot in orientation angle and extended transient.

This leads to the rather depressing conclusion that while the Hinch–Leal closure may be considerably more accurate than the pre-averaged closure at predicting the gross features of the flows we have considered, it appears to be far more susceptible to non-physical behaviour, at least in uniform shear flow. One can only speculate what may be the implications of this sort of non-physical behaviour for the delicate numerical calculations that make use of closure approximations in solving flow problems for microstructured fluids.

6. Conclusions

In I we proposed a new class of computational techniques for flow problems of microstructured fluids. This idea is based on a Lagrangian representation of the evolution equation for the distribution function of the conformation of the microstructure; this representation is exactly equivalent to the conventional Eulerian representation (the Fokker–Planck or Smoluchowski or Forward–Kolmogorov equation), from which it may be derived. This alternative point of view allows one to reformulate the equations that govern the macroscopic mechanics and microscopic physics of microstructured fluids. The result is a computational method in which the macroscopic mechanics are accounted for using a standard Eulerian technique, and the microscopic physics are accounted for using Lagrangian marker particles that evolve in a way that reflects the evolution of the associated distribution function.

In this paper, we have pursued a realization of this idea in the form of a computational technique for the solution of flow problems of dilute suspensions of rigid, orientable particles in a Newtonian carrier fluid. The numerical technique is presented in full detail. We carried out example calculations for the pressure-driven flow of the suspension between parallel flat plates. These calculations revealed the first and second Newtonian regimes at low and high Péclet numbers, respectively, and also the shear-thinning behaviour exhibited by suspensions between these two regimes. We compared our results with those one can obtain using two commonly made closure approximations, the quadratic closure and the Hinch–Leal composite closure. For the suspensions of particles of moderate aspect ratio that we considered, the closure models tended to predict normalized flow rate deficits due to the addition of the particles to within, at worst, 10–30%. Asymptotic results indicated that the quadratic closure predicted shear-thinning behaviour that is too dramatic compared to that shown by the full equations. The Hinch–Leal closure was considerably better in this regard.

During the integrations of the closure models, it was observed that non-physical negative diagonal components of the second moment arose during the integration of the Hinch–Leal closure. This was shown by way of example for a uniform shear calculation at moderately large Péclet number. A simple geometrical analysis of the moment evolution equations derived using the two closure models showed that such non-physical moments are a common possibility, at least during transient response. Hence, use of moment components to deduce dominant particle orientations is highly suspect when using a closure approximation.

In the final analysis, the numerical algorithm we presented has certain advantages

and disadvantages when compared to other, available methods. To begin, we wish to note several advantages relative to brute-force integration of the associated Fokker–Planck equation. Our technique requires far fewer unknowns, as a consequence of the self-adaptive nature of the algorithm, as discussed in detail in Appendix B. Secondly, when the Brownian diffusivity is set to zero, there can be no false diffusion associated with solutions obtained by our new technique. Brute-force integration of the Fokker–Planck equation, however, will suffer from false diffusion whether the Brownian diffusivity is zero or positive. The reason is that one must discretize a convective derivative if one solves the Eulerian formulation of the Fokker–Planck equation.

Next, we compare our technique to direct integration of moment evolution equations derived using a closure approximation. A disadvantage of our method is that the equations derived using the double-Lagrangian technique are considerably more complicated than moment evolution equations derived with a closure approximation. In addition, integration of the full equations by our new technique on the computer is slower than the integration of moment evolution equations; however, when the Brownian diffusivity is zero (as it is for larger particles), this difference is negligible. A disadvantage of closure models that we demonstrated was that even in our relatively mild test, the closure models can give results that are in error. Perhaps more importantly, transient behaviour of closure models can be quite different from that of the full equations. This may lead to instabilities in numerical calculations of closure models that are artifacts of the closure approximation itself.

In addition, we demonstrated that even in uniform steady shear flow, the closure models can lead to non-physical negative diagonal components of the moment of the distribution function. Thus, if one wishes to connect observed, macroscopic non-Newtonian behaviour of the suspension to dynamics of particles carried by the flow, one cannot use the closure models we examined. The goal of a phenomenological model for a microstructured fluid is, after all, an assembly of the well-understood microscale dynamics of the local structure into a coherent picture of the macroscopic behaviour of the material. We have demonstrated that while closure approximations can give results that are not too terrible in a realistic flow, the connection between microscale and macroscale behaviour is at best obscured by their use.

Appendix A. An alternative discretization of the coordinate map that fails

Owing to the fact that the coordinate map is a map of the sphere of orientations, it would seem natural to solve for $\boldsymbol{R}(t;\boldsymbol{R}_0)$ in terms of spherical polar coordinates. In other words, one could attempt to find the map

$$(\sigma_0,\theta_0)\mapsto(\sigma(t;\sigma_0,\theta_0),\theta(t;\sigma_0,\theta_0)),$$

where (σ,θ) are the modified spherical polar coordinates defined in figure 1, say. This approach leads to evolution equations for $\sigma(t:\sigma_0,\theta_0)$ and $\theta(t;\sigma_0,\theta_0)$, as follows. First, we have the Cartesian components of the director

$$\boldsymbol{R}=\begin{pmatrix}\cos\theta\cos\sigma\\ \cos\theta\sin\sigma\\ \sin\theta\end{pmatrix}$$

and the identity

$$\dot{\boldsymbol{R}}=\dot{\sigma}\cos\theta\boldsymbol{e}_\sigma+\dot{\theta}\boldsymbol{e}_\theta.$$

The distribution function in these coordinates may be written

$$\frac{f^*(t;\sigma_0,\theta_0)}{f^*(0;\sigma_0,\theta_0)} = \left[\frac{\partial(\sigma,\theta)}{\partial(\sigma_0,\theta_0)}\frac{\cos\theta}{\cos\theta_0}\right]^{-1}. \tag{A 1}$$

The angles (σ_0, θ_0) serve as coordinates in the reference configuration, while the angles (σ, θ) are coordinates in the deformed configuration. We have used the notation

$$\frac{\partial(\sigma,\theta)}{\partial(\sigma_0,\theta_0)} \equiv \frac{\partial\sigma}{\partial\sigma_0}\frac{\partial\theta}{\partial\theta_0} - \frac{\partial\sigma}{\partial\theta_0}\frac{\partial\theta}{\partial\sigma_0}.$$

By using the Lagrangian representation for the distribution function (A 1), the Brownian term may be reformulated as discussed at length in I. This procedure yields a closed set of evolution equations for the coordinate map from reference to deformed configurations of the suspended phase written here for the case of unidirectional flow:

$$\frac{\partial}{\partial t}\sigma = \frac{1}{2}\frac{\partial u}{\partial y} + \frac{G}{2}\frac{\partial u}{\partial y}\cos 2\sigma - \frac{D_R}{\cos\theta\cos\theta_0}\frac{\partial(\cdot,\theta)}{\partial(\sigma_0,\theta_0)}\left(\frac{\partial(\sigma,\theta)}{\partial(\sigma_0,\theta_0)}\frac{\cos\theta}{\cos\theta_0}\right), \tag{A 2a}$$

$$\frac{\partial}{\partial t}\theta = -\frac{G}{4}\frac{\partial u}{\partial y}\sin 2\sigma\sin 2\theta - D_R\frac{\cos\theta}{\cos\theta_0}\frac{\partial(\sigma,\cdot)}{\partial(\sigma_0,\theta_0)}\left(\frac{\partial(\sigma,\theta)}{\partial(\sigma_0,\theta_0)}\frac{\cos\theta}{\cos\theta_0}\right). \tag{A 2b}$$

The coordinate map we seek is therefore the solution to (A 2); however, the numerical solution of these equations is fraught with difficulty, owing to the singularity in the coordinate system at the poles ($\theta = \pm\frac{1}{2}\pi$). In particular, the $1/\cos\theta$ factor in the Brownian term of (A 2*a*) becomes problematic as one approaches a pole of the sphere of orientations. Moreover, this factor multiplies the most important source of nonlinearity in the system (A 2). The consequence of these observations is that, as one refines the discretization of the system, one is restricted to very small time steps required for stable integration. Clearly the source of the restriction is but an artifact of the coordinate system. Therefore, we use Cartesian coordinates for orientation space, as described.

Appendix B. Tests of the numerical technique

The numerical method for integration of the orientation distribution was tested by computation of uniform shear flow. In particular, we were interested in what is the required discretization of the sphere of orientations, depending on the Brownian diffusivity and on the shear rate.

As a consequence of the special nature of the flow, it is possible to rescale time by the shear rate $\dot{\gamma}$. Thus there is only a single parameter characterizing the solution, $\dot{\gamma}/D_R = Pe$ (the Péclet number). For various values of Pe we computed the orientation dynamics of a single ensemble of particles by the new technique. Then we compared the particle contribution to the shear stress, and the first and second normal stress differences. These time traces were compared for various discretizations of the sphere of orientations (3.2). We found no visible improvement in the solution was obtained when j_{max} exceeded the recommended values shown in table 1.

In practice, when computing the inhomogeneous flows that we discuss in the main body of the paper, we found the following results concerning execution time on a Convex 240 supercomputer. Almost all the execution time is spent updating the orientations of particles. In scalar execution mode, for a single predictor-corrector step to be computed for a single ensemble of discretization $j_{max} = 20$ requires approximately 350 ms of CPU time. Vectorization improved this result to 150 ms of CPU time/time-

Pe	j_{max}	Number of unknowns	Δt
100	15	256	0.00625
10	15	256	0.0125
1	20	441	0.00125

TABLE 1. Recommended discretization and time-step sizes

step/ensemble. Finally, the code was found to profit from parallelization when there are many ensembles, as each ensemble can be updated simultaneously and independently by a different, dedicated processor. The parallel efficiency (speed-up/number of processors) was 68%. Thus a single predictor-corrector step for a single ensemble with $j_{max} = 20$ required approximately 50 ms of clock time on a 4 processor machine. For $j_{max} = 15$, these times are reduced by 50%.

The recommended discretizations we report should be compared with the discretizations required by Kamal & Mutel (1989) in a recent numerical solution of the Fokker–Planck equation for the distribution function in a suspension of rigid particles under uniform shear. They made use of finite differences and a cyclic tridiagonal matrix algorithm to solve for the distribution function using 7745 unknowns for a single ensemble. No information concerning time-step size or execution time was given in their paper.

REFERENCES

ADVANI, S. G. & TUCKER, C. L. 1987 The use of tensors to describe and predict fiber orientation in short fiber composites. *J. Rheol.* **31**, 751–784.

ADVANI, S. G. & TUCKER, C. L. 1990 Closure approximations for three-dimensional structure tensors. *J. Rheol.* **34**, 367–386.

ALTAN, M. C., ADVANI, S. G., GÜÇERI, S. I. & PIPES, R. B. 1989 On the description of the orientation state for fiber suspensions in homogeneous flows. *J. Rheol.* **33**, 1129–1155.

BIRD, R. B., HASSAGER, O., ARMSTRONG, R. C. & CURTISS, C. F. 1987 *Dynamics of Polymeric Liquids; Vol. 2, Kinetic Theory*. John Wiley and Sons.

BRETHERTON, F. P. 1962 The motion of rigid particles in a shear flow at low Reynolds number. *J. Fluid Mech.* **14**, 284–304.

DINGMAN, S. E. 1992 Three dimensional simulation of fluid particle interactions using the boundary element method. PhD dissertation, University of New Mexico.

EL-KAREH, A. & LEAL, L. G. 1989 Existence of solutions for all Deborah numbers for a non-Newtonian model modified to include diffusion. *J. Non-Newtonian Fluid Mech.* **33**, 257–287.

FRATTINI, P. L. & FULLER, G. G. 1986 Rheo-optical studies of the effect of weak Brownian rotations in sheared suspensions. *J. Fluid Mech.* **168**, 119–150.

GIESEKUS, H. 1962 Elasto-viskose Flüssigkeiten, für die in stationären Schichtströmungen sämtliche Normalspannungskomponenten verschieden gtroß sind. *Rheologica Acta* **2**, 50–62.

HINCH, E. J. & LEAL, L. G. 1973 Time-dependent shear flows of a suspension of particles with weak Brownian rotations. *J. Fluid Mech.* **57**, 753–767.

HINCH, E. J. & LEAL, L. G. 1975 Constitutive equations in suspension mechanics. Part 1. General Formulation. *J. Fluid Mech.* **71**, 481–495.

HINCH, E. J. & LEAL, L. G. 1976 Constitutive equations in suspension mechanics. Part 2. Approximate forms for a suspension of rigid particles affected by Brownian rotations. *J. Fluid Mech.* **76**, 187–208.

JEFFERY, G. B. 1922 The motion of ellipsoidal particles immersed in a fluid. *Proc. R. Soc. Lond.* A **102**, 161–179.

KAMAL, M. R. & MUTEL, A. T. 1989 The prediction of flow and orientation behavior of short fiber reinforced melts in simple flow systems. *Polymer Composites* **10**, 337–343.

KUZUU, N. Y. & DOI, M. 1980 Nonlinear viscosity of concentrated solutions of rod-like polymers. *Polymer J.* **12**, 883–890.

LARSON, R. G. 1988 *Constitutive Equations for Polymer Melts and Solutions.* Butterworth.

LEAL, L. G. & HINCH, E. J. 1971 The effect of weak Brownian rotations on particles in shear flow. *J. Fluid Mech.* **46**, 685–703.

LEAL, L. G. & HINCH, E. J. 1972 The rheology of a suspension of nearly spherical particles subject to Brownian rotations. *J. Fluid Mech.* **55**, 745–765.

LIPSCOMB, G. G., DENN, M. M., HUR, D. U. & BOGER, D. V. 1988 The flow of fiber suspensions in complex geometries. *J. Non-Newtonian Fluid Mech.* **26**, 297–325.

OKAGAWA, A., COX, R. G. & MASON, S. G. 1973 The kinetics of flowing dispersions. VI. Transient orientation and rheological phenomena of rods and discs in shear flow. *J. Colloid Interface Sci.* **45**, 303–329.

SZERI, A. J. & LEAL, L. G. 1992 A new computational method for the solution of flow problems of microstructured fluids. Part 1. Theory. *J. Fluid Mech.* **242**, 549–576 (referred to herein as I).

SZERI, A. J. & LEAL, L. G. 1993 Microstructure suspended in three-dimensional flows. *J. Fluid Mech.* **250**, 143–167.

SZERI, A. J., MILLIKEN, W. & LEAL, L. G. 1992 Rigid particles suspended in time-dependent flows: irregular versus regular motion, disorder versus order. *J. Fluid Mech.* **237**, 33–56.

SZERI, A. J., WIGGINS, S. & LEAL, L. G. 1991 On the dynamics of suspended microstructure in unsteady, spatially inhomogeneous, two-dimensional fluid flows. *J. Fluid Mech.* **228**, 207–241.